

---

## Direct numerical simulation of a $30R$ long turbulent pipe flow at $R^+ = 685$ : large- and very large-scale motions

Xiaohua Wu, J. R. Baltzer and R. J. Adrian

Journal of Fluid Mechanics / Volume 698 / May 2012, pp 235 - 281

DOI: 10.1017/jfm.2012.81, Published online: 05 April 2012

**Link to this article:** [http://journals.cambridge.org/abstract\\_S002211201200081X](http://journals.cambridge.org/abstract_S002211201200081X)

### How to cite this article:

Xiaohua Wu, J. R. Baltzer and R. J. Adrian (2012). Direct numerical simulation of a  $30R$  long turbulent pipe flow at  $R^+ = 685$ : large- and very large-scale motions. Journal of Fluid Mechanics, 698, pp 235-281 doi:10.1017/jfm.2012.81

**Request Permissions :** [Click here](#)

# Direct numerical simulation of a $30R$ long turbulent pipe flow at $R^+ = 685$ : large- and very large-scale motions

Xiaohua Wu<sup>1</sup>, J. R. Baltzer<sup>2</sup> and R. J. Adrian<sup>2†</sup>

<sup>1</sup> Department of Mechanical Engineering, Royal Military College of Canada, Kingston, Ontario, K7K 7B4, Canada

<sup>2</sup> School for Engineering of Matter, Transport and Energy, Arizona State University, PO Box 876106, Tempe, AZ 85287-6106, USA

(Received 23 May 2011; revised 30 January 2012; accepted 6 February 2012;  
first published online 5 April 2012)

Fully developed incompressible turbulent pipe flow at Reynolds number  $Re_D = 24\,580$  (based on bulk velocity) and Kármán number  $R^+ = 684.8$  is simulated in a periodic domain with a length of 30 pipe radii  $R$ . While single-point statistics match closely with experimental measurements, questions have been raised of whether streamwise energy spectra calculated from spatial data agree with the well-known bimodal spectrum shape in premultiplied spectra produced by experiments using Taylor's hypothesis. The simulation supports the importance of large- and very large-scale motions (VLSMs, with streamwise wavelengths exceeding  $3R$ ). Wavenumber spectral analysis shows evidence of a weak peak or flat region associated with VLSMs, independent of Taylor's hypothesis, and comparisons with experimental spectra are consistent with recent findings (del Álamo & Jiménez, *J. Fluid Mech.*, vol. 640, 2009, pp. 5–26) that the long-wavelength streamwise velocity energy peak is overestimated when Taylor's hypothesis is used. Yet, the spectrum behaviour retains otherwise similar properties to those documented based on experiment. The spectra also reveal the importance of motions of long streamwise length to the  $uu$  energy and  $uv$  Reynolds stress and support the general conclusions regarding these quantities formed using experimental measurements. Space–time correlations demonstrate that low-level correlations involving very large scales persist over  $40R/U_{bulk}$  in time and indicate that these motions convect at approximately the bulk velocity, including within the region approaching the wall. These very large streamwise motions are also observed to accelerate the flow near the wall based on force spectra, whereas smaller scales tend to decelerate the mean streamwise flow profile, in accordance with the behaviour observed in net force spectra of prior experiments. Net force spectra are resolved for the first time in the buffer layer and reveal an unexpectedly complex structure.

**Key words:** pipe flow boundary layer, turbulent boundary layers

---

## 1. Introduction

The importance of motions with very long streamwise extent in incompressible, fully-developed, turbulent pipe flow was brought into focus more than a decade ago

† Email address for correspondence: [rjadrian@asu.edu](mailto:rjadrian@asu.edu)

by Kim & Adrian (1999), hereafter referred to as KA99. Using premultiplied, one-dimensional spectra of the streamwise velocity fluctuation, they found that modes of streamwise wavelength significantly longer than one pipe radius make substantial contributions to streamwise turbulent kinetic energy at moderate Reynolds numbers. KA99 observed that premultiplied streamwise velocity spectra exhibit two maxima, suggestive of a bimodal form. One maximum exists at the low-wavenumber end of the inertial subrange, which KA99 associated with large-scale motions (LSMs) with length of the order of a few pipe radii  $R$ , and the other exists at longer wavelength. The latter scales were called ‘very large-scale motions’ (VLSMs). LSMs were originally identified as turbulent bulges in turbulent boundary layers, with the average dimensions of bulges accepted to be  $2\text{--}3\delta$  in streamwise length,  $1\text{--}1.5\delta$  in width, and  $\delta$  in height (reviewed in Guala, Hommema & Adrian 2006). It has become conventional to define LSMs with these nominal dimensions for the canonical wall shear flows, where  $\delta$  is the appropriate length scale of channel half-height  $h$ , pipe radius  $R$ , or boundary layer thickness  $\delta$ . The short-wavelength boundary of LSMs depends on Reynolds number, but at typical laboratory Reynolds numbers is about the thickness of the logarithmic layer or slightly longer ( $0.2\text{--}0.3\delta$ ). It is convenient to define LSMs as wavelengths up to  $3\delta$  and define VLSMs as longer wavelengths, but this is nominal and may be subject to change in the light of future findings.

In pipe flow experiments at significantly higher Reynolds numbers than the present simulation, Guala *et al.* (2006) have calculated that VLSMs with streamwise length greater than  $3R$  contain over 65 % of the streamwise turbulent kinetic energy at the radii they measured. The bimodal form has also been observed in turbulent channels and boundary layers (for example, Hites 1997; Balakumar & Adrian 2007). The wavelengths at which peaks occur as a function of wall-normal position from various experiments are summarized in figure 1. The wavelengths of long-wavelength flattened regions or peaks for the present simulation are also included in the plot along with peak locations from a pipe experiment with similar Reynolds number (Hultmark, Bailey & Smits 2010), and these are discussed in § 4.2.

The preceding spectrum results and others (such as Monty *et al.* 2007; Bailey *et al.* 2008) are based on experimental investigations with hot wires or films, which require Taylor’s hypothesis (Taylor 1938) to estimate the spatial behaviour based on single-point temporal measurements. More recently, doubts have been raised regarding the presence of the bimodal behaviour in spectra obtained from Fourier transforms of true spatial fields without the use of Taylor’s hypothesis. del Álamo & Jiménez (2009) (see also Moin 2009) discussed the convection velocities of motions of various streamwise wavelengths in turbulent channel flow, and found that long-wavelength motions moving faster than the local mean lead to errors when Taylor’s hypothesis is invoked, particularly in the buffer and inner logarithmic layers. They showed that the long-wavelength peak for a turbulent channel is clearly present when Taylor’s hypothesis is used, but suggest that the energy spectrum based on purely spatial information could behave more similar to  $k_x^{-1}$ , where  $k_x$  is the streamwise wavenumber, making the peak at least partially an artifact due to Taylor’s hypothesis. Their study followed a comparison between direct numerical simulations (DNS) and hot-wire measurements of a turbulent channel at  $Re_\tau \approx 1000$  by Monty & Chong (2009), who noted the absence of a DNS longer-wavelength spectrum peak, finding the shape more similar to a shoulder. del Álamo & Jiménez (2009) also compared  $Re_\tau = 2000$  channel DNS spectra modified to simulate the effects of using Taylor’s hypothesis with experimental measurements of a pipe. They also indicated the peak induced by Taylor’s hypothesis would become stronger with increasing Reynolds number.

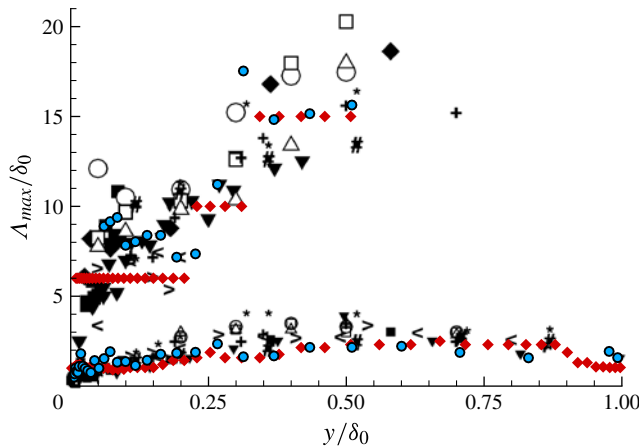


FIGURE 1. Comparison of wavelengths for spectral peaks in premultiplied streamwise velocity energy spectra for the present DNS and various experiments as a function of wall-normal distance. Data from the present  $R^+ = 685$  simulation are included (smaller red diamonds), and all other data are obtained from experiment. The small circles with blue centres are obtained from the hot-wire spectra of Hultmark *et al.* (2010) for  $R^+ = 690$  pipe flow. Other data are adapted from Balakumar & Adrian (2007): ‘Hash symbol,  $Re_\tau = 531$  (channel); plus symbol,  $Re_\tau = 960$  (channel); asterisk symbol,  $Re_\tau = 1584$  (channel); less than symbol,  $Re_\tau = 1476$  (ZPGBL); and greater than symbol,  $Re_\tau = 2395$  (ZPGBL)’. The remaining symbols correspond to pipes, mainly at considerably higher Reynolds number than the present simulation, including Guala *et al.* (2006) at  $\circ$ ,  $R^+ = 3815$ ;  $\square$ ,  $R^+ = 5884$ ;  $\triangle$ ,  $R^+ = 7959$ ; and  $\blacklozenge$ , Bullock, Cooper & Abernathy (1978) at  $R^+ = 2630$ . The other symbols are defined in figure 4 of Guala *et al.* (2006).

Similar studies directly comparing experimental and DNS pipe flows at sufficiently high Reynolds numbers to observe this effect have not been performed.

While DNS of turbulent channels have been performed in long streamwise domains at increasingly high Reynolds numbers (del Álamo *et al.* 2004; Hoyas & Jiménez 2006), there has been a distinct absence of DNS to study very long structures in pipe flow. In this paper we present the first DNS evidence of very long coherent structures in fully-developed turbulent pipe flow. Previous pipe flow DNS studies mostly dealt with the mean and second-order turbulent statistics, e.g. Eggels *et al.* (1994) and Wu & Moin (2008). The axial dimensions of the computational domains used in those simulations were no more than  $15R$ . Chin *et al.* (2010) examined the effect of DNS pipe simulation length on statistics and also considered energy spectra, but the maximum Reynolds number was  $R^+ = 500$ , and they concluded that no outer peak was discernible in premultiplied spectrum maps, which present the premultiplied spectra over a range of  $y$  (wall-normal position) values. The present simulation adopts an axial dimension of  $30R$ . It is the first DNS study focusing on the very long structures in fully-developed turbulent pipe flow at this high of Reynolds number. In comparing pipe DNS statistics for varying streamwise lengths, Chin *et al.* (2010) found that the one-dimensional energy spectrum was the statistic that required the greatest length, and lengths of  $8\pi R$  were adequate for the Reynolds numbers they considered. The longest channel simulations of del Álamo *et al.* (2004) and Hoyas & Jiménez (2006) also used computational domains with lengths of  $8\pi$  times the channel half-height,

so our domain accommodates similar motions and is of sufficient length for correct statistics based on the observations of Chin *et al.* (2010).

Guala *et al.* (2006) also experimentally observed the importance of VLSM contributions in turbulent pipe flows, with VLSMs contributing 50–60% of the Reynolds shear stress at the radii they measured. The importance of VLSMs in carrying  $uv$  Reynolds stress was unexpected based on the idea originally inferred by Townsend (1976) that the very long motions would be inactive, that is, would carry substantial  $uu$  energy but little Reynolds stress. del Álamo & Jiménez (2001) and del Álamo & Jiménez (2003) had also previously observed the sizable contributions of very long motions to  $uv$  Reynolds stress in turbulent channel simulations, and del Álamo *et al.* (2004) found that these contributions occur mainly in the outer region and that this is how the impermeability of the wall limits the wall-normal motions in relation to Townsend's idea. Through experimental particle image velocimetry measurements in channels, Liu, Adrian & Hanratty (2001) also showed that relatively long streamwise scales carried substantial  $uv$  without requiring Taylor's hypothesis, but the maximum streamwise spatial length that they could observe was limited. Guala *et al.* (2006) also used  $uv$  spectra to compute net force spectra that decompose a Reynolds stress term that appears in the mean momentum equation into contributions by streamwise wavenumber. They found that VLSMs played a special role because the net force contribution of these wavelengths changed sign to accelerate the streamwise flow as the wall was approached, but measurements were made no closer than  $0.15R$  from the wall. The  $uv$  spectral contributions will therefore be quantified for the present pipe simulation, and the DNS will permit computing force spectra without error introduced from the use of Taylor's hypothesis and with positions nearer to the pipe wall available.

The organization of the present study is as follows: after verifying that single-point statistics are in agreement with experiments and documenting additional statistics characterizing the simulation, we compare energy spectra with experimental measurements and observe the significant amount of energy in very long scales for the simulation (§4). We proceed by discussing the axial wavelengths at which particular cumulative energy fractions occur in the light of prior experimental observations (§4.3). Having established the significance of these motions in the present simulation and observed similarities and differences with experiments, we visualize contours of axial velocity fluctuation and then filter them to concentrate on the VLSMs (§5). Observations from the time evolution of these fields are then related to space–time correlations (§6) and the convection velocity of very long streamwise modes (§7). Having characterized these properties of very long motions in this pipe simulation, we conclude by examining the net force spectra (§8) and summarizing the results.

## 2. Computational details

In the present study, the unit length scale is the pipe radius  $R$ , and the unit velocity scale is  $U_{bulk}$ , which is defined as the ratio of mean volume flow rate and pipe cross-sectional area. The unit time scale is therefore  $R/U_{bulk}$ . The Reynolds number based on pipe diameter  $D$  and  $U_{bulk}$ ,  $Re_D = 24\,580$ , is the same as that in the experiments of den Toonder & Nieuwstadt (1997). Superscript  $+$  refers to quantities normalized by friction velocity  $u_\tau$  for velocity and by viscous wall unit  $\nu/u_\tau$  for distance. The Kármán number  $R^+$  is equivalent to the friction Reynolds number  $Re_\tau$ , but here the former is reserved for pipe flows while the latter is generally used for other wall-bounded shear flows.

$r$  is the radial coordinate measured from pipe axis,  $x$  is the flow axial direction, and  $\theta$  is the azimuthal coordinate. For the purpose of analogy with the spanwise coordinate of a channel, we introduce the arclength  $s = r\theta$ . (The use of arclength in turbulent pipe flows is discussed by Monty *et al.* 2007.) By analogy with the wall-normal coordinate of a channel, it is also convenient to define  $y = R - r$  for the pipe (also used by Guala *et al.* 2006). It is also helpful to introduce the analogous velocity components  $u = u_x$ ,  $v = -u_r$ , and  $w = u_\theta$ . The subscripts of correlation functions herein use  $u$ ,  $v$ ,  $w$  to indicate the velocity components.

The finite-difference grid size used in the current computation is  $256 \times 1024 \times 2048$  along the  $r$ ,  $\theta$ , and  $x$  directions, respectively. Resolution along the axial direction is  $\Delta x^+ = 10.03$  or  $\Delta x = 0.00732R$ . The computed pipe radius and friction velocity based Kármán number  $R^+$  is 684.8. Along the azimuthal direction maximum grid spacing is achieved at the wall ( $r = R$ ) yielding  $\Delta(R\theta)^+ = 4.2$ . The minimum and maximum wall-normal grid spacings are  $3.578 \times 10^{-4}R$  and  $9.892 \times 10^{-3}R$ , respectively. In wall units, these correspond to 0.144 and 11.3. The maximum wall-normal grid spacing is located at  $r = 0.406R$  rather than at the centreline. The first layer of grid points in the staggered mesh system is located 0.205 wall units from the pipe surface. There are 108 grid points located near the wall between  $0 < y/R < 0.1$ , and 44 grid points near the centreline between  $0.9 < y/R < 1.0$ . At the pipe centreline the wall-normal grid spacing is  $1.435 \times 10^{-3}R$ . Below  $y^+ = 50$ , the wall-normal grid spacing  $\Delta r^+$  is 1.2 or less, and below  $y^+ = 30$ ,  $\Delta r^+ < 0.8$ .

The computer program, numerical method and boundary conditions are the same as those described in Wu & Moin (2008). The simulation was performed using 160 threads on a Sun SPARC Enterprise M9000 Server. Each restart data file has a size of 21.7 GB. Except for an initial start-up period, the computational time step was fixed at  $\Delta t = 0.009R/U_{bulk}$ . The initial condition was plug flow superimposed with a random number field. The simulation was first advanced for  $300R/U_{bulk}$ . Statistics were subsequently collected for another  $260R/U_{bulk}$ . An overbar represents averaging over time as well as over the two homogeneous directions.

### 3. Validation of DNS results

To establish the validity of the simulation, one- and two-point statistics are compared to experimental data. Figure 2(a) compares the DNS profile of  $\bar{u}^+$  as a function of  $y^+$  with the experimental data of den Toonder & Nieuwstadt (1997). To document additional aspects of the mean velocity for the present DNS, profiles of the mean velocity gradient, the logarithmic-law indicator function, and the power-law indicator function are plotted in figure 2(b). The indicator functions for a Wu & Moin (2008) pipe simulation at  $Re_D = 44\,000$  (but shorter domain length) are included for comparison, as the higher Reynolds number flow would be expected to possess a wider region that could obey such a law. Interpretation of the indicator functions and their relation to scaling laws are discussed therein. Wu & Moin (2008) noted that at low Reynolds numbers (including their pipe DNS) the narrow logarithmic slope region was not the same as what was implied by the classical complete similarity arguments.  $d\bar{u}/dy$  experiences a precipitous drop within the buffer region and its curvature changes from convex (viscous sublayer) to concave and back to convex (core region).  $d\bar{u}^+/d\ln(y^+)$  is approximately constant over the region of  $40 < y^+ < 100$ , indicating an approximately logarithmic dependence of  $\bar{u}^+$  on  $y^+$ . This region is narrower than that of the higher Reynolds number simulation, but the overall behaviour is very similar. The comparison between the power-law indicator functions  $d\ln(\bar{u}^+)/d\ln(y^+)$  for the present pipe simulation and the  $Re_D = 44\,000$  simulation also indicates a narrower flat

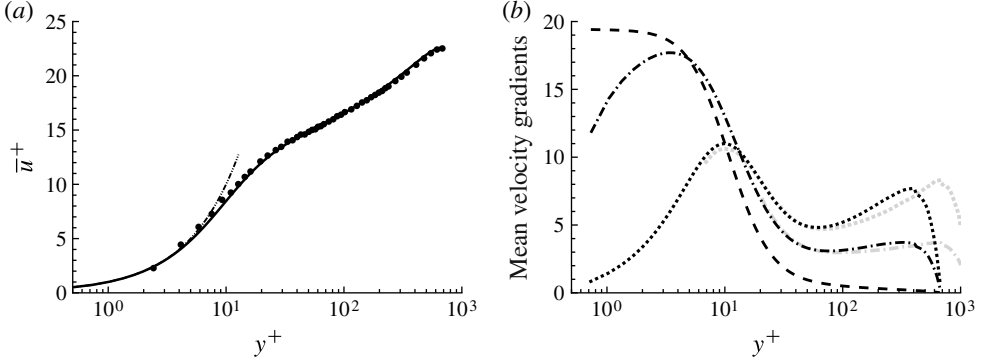


FIGURE 2. (a) Mean velocity as a function of  $y^+$ . Symbols: den Toonder & Nieuwstadt (1997); solid line: present DNS; dash-double dotted line:  $\bar{u}^+ = y^+$ . (b) Mean velocity gradients as a function of  $y^+$  for the present DNS. Dashed line:  $0.5(R/U_{bulk}) d\bar{u}/dy$ ; dotted line:  $2 d\bar{u}^+/d\ln(y^+)$ ; dash-dotted line:  $20 d\ln(\bar{u}^+)/d\ln(y^+)$ . The light grey lines are for the  $Re_D = 44000$  pipe DNS of Wu & Moin (2008).

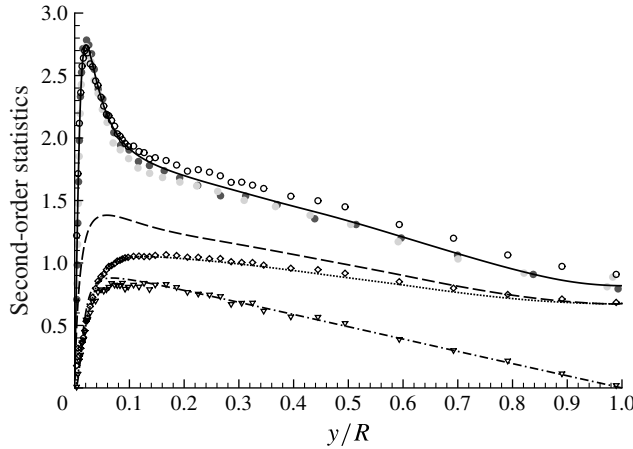


FIGURE 3. Turbulence intensities and shear stress as a function of  $y/R$ . Open symbols: den Toonder & Nieuwstadt (1997); filled dots: Hultmark *et al.* (2010) at  $Re_D = 24100$  with hot-wire length  $l_w^+ = 4.3$  (dark) and  $Re_D = 23800$  with  $l_w^+ = 19.1$  (light grey); lines: present DNS. Solid line:  $u'_{x,rms} u'_{x,rms}$ ; dashed line:  $u'_{\theta,rms} u'_{\theta,rms}$ ; dotted line:  $u'_{r,rms} u'_{r,rms}$ ; dash-dotted line:  $\overline{u'_x u'_r}$ .

region of adherence to power-type behaviour, where Wu & Moin (2008) found this region was already limited to  $70 < y^+ < 120$  for the higher Reynolds number.

The second-order turbulence statistics are compared with those of den Toonder & Nieuwstadt (1997) in figure 3. The comparison of  $u'_{x,rms} u'_{x,rms}$  also includes hot-wire data obtained by Hultmark *et al.* (2010). The near-wall peaks are very similar in magnitude and location for the experiments and the DNS. In the DNS data, the  $u'_{x,rms} u'_{x,rms}$ ,  $u'_{r,rms} u'_{r,rms}$  and  $u'_{\theta,rms} u'_{\theta,rms}$  peaks occur at  $y^+ = 14$ , 86 and 41, respectively. The  $\overline{u'_x u'_r}$  peak occurs at  $y^+ = 47$ , which agrees closely with the value of  $y^+ = 52$  from the correlation of the location of maximum Reynolds shear stress for pipes and channels  $y_{RS,max} \approx 2(Re_\tau)^{1/2}$  (Sreenivasan 1987; Sreenivasan & Sahay 1997; Marusic *et al.* 2010). The values



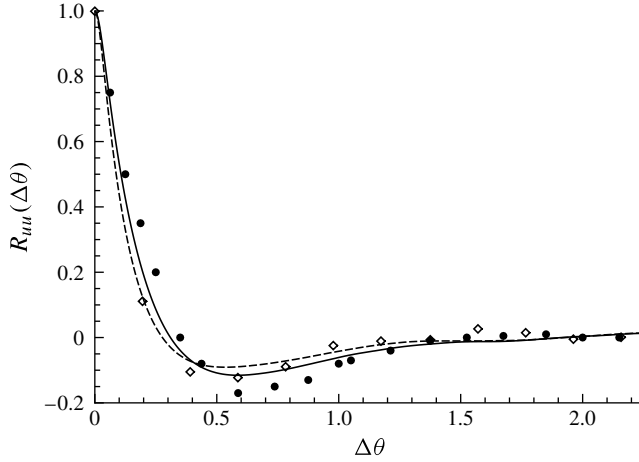


FIGURE 4. Two-point correlation coefficient  $R_{uu}$  as a function of azimuthal separation  $\Delta\theta$ . Filled circles: Bailey *et al.* (2008) at  $y/R = 0.2$  for  $Re_D = 76\,000$ ; open diamonds: Monty *et al.* (2007) at  $y/R = 0.15$  for  $Re_D = 21\,400$  ( $R^+ = 615$ ); solid line: present DNS at  $y/R = 0.2$ ; dashed line: present DNS at  $y/R = 0.15$ .

of  $u'_{x,rms}^+$  in the region above the peak to the pipe centreline are appreciably larger in den Toonder & Nieuwstadt (1997) than those of Hultmark *et al.* (2010) and the DNS. Experimental data of the Reynolds shear stress are noisy and measurements of the azimuthal turbulent intensity are not available. The maximum deviation of the DNS total shear stress  $\left(-\nu d\bar{u}_x/dr + \overline{u'_x u'_r}\right)^+$  relative to the local theoretical linear value  $r/R$  is 2.27 %. Figure 3 shows that for  $0.9 < y/R < 1.0$  near the pipe axis the azimuthal and radial turbulent intensity profiles collapse. This Reynolds-number-independent feature is dictated by the Reynolds-averaged mean radial momentum transport equation

$$-\frac{1}{\rho} \frac{\partial \bar{p}}{\partial r} - \frac{\overline{u_r'^2} - \overline{u_\theta'^2}}{r} - \frac{d\overline{u_r'^2}}{dr} = 0, \quad (3.1)$$

and serves as an additional check of the simulation quality.

The two-point correlation coefficient  $R_{uu}$  as a function of azimuthal separation  $\Delta\theta$  is compared with the experimental data of Monty *et al.* (2007) and Bailey *et al.* (2008) at two radial locations in figure 4. Here  $R_{uu}$  represents correlation of the axial velocity component at two locations. The Reynolds number of Bailey *et al.* (2008) shown in the figure is more than three times the present value. However, Bailey *et al.* (2008) showed that  $R_{uu}(\Delta\theta)$  remains nearly frozen over a two-order magnitude range in  $Re_D$ . Monty *et al.* (2007) also showed that  $R_{uu}(\Delta\theta)$  is insensitive to the change of Reynolds number. Overall, evaluations of the two-point correlation coefficient, mean and second-order statistics validate the statistical features of the present DNS.

## 4. Energy spectra

### 4.1. Definitions

For clarity, the definitions and normalization conventions of energy are summarized below; these are generally consistent with other literature, such as Guala *et al.* (2006), in which more detail is given. Following common usage, the plots and



discussion use the velocity components instead of their number indices as subscripts of correlation  $R$  and energy spectrum  $\Phi$ ; however, numerical index subscripts are more convenient in these equations. Given the two-point streamwise correlation  $R_{ij}(r_x; y) = \langle u'_i(x, y)u'_j(x + r_x, y) \rangle$  (with averaging over  $\theta$  and time implicitly assumed), the co-spectrum is defined as

$$S_{ij}(k_x; y) \equiv \frac{1}{2\pi} \int_{-\infty}^{\infty} e^{-\sqrt{-1}k_x r_x} R_{ij}(r_x; y) dr_x, \quad (4.1)$$

which is the Fourier transform of the correlation. Then the one-sided wavenumber co-spectrum is given by

$$\Phi_{ij}(k_x; y) = S_{ij}(k_x; y) + S_{ij}(-k_x; y) = 2\text{Re} \{ S_{ij}(k_x; y) \}. \quad (4.2)$$

The spectra are related to the mean-square fluctuation by

$$\overline{u'_i u'_j} = \int_{-\infty}^{\infty} S_{ij}(k_x) dk_x = \int_0^{\infty} \Phi_{ij}(k_x) dk_x. \quad (4.3)$$

The computed spectra (via discrete Fourier transforms) are normalized to discretely approximate (4.3) such that

$$\overline{u'_i u'_j} = \sum_{n_x=-N_x/2+1}^{N_x/2} S_{ij}(n_x) \Delta k_x = \sum_{n_x=0}^{N_x/2} \Phi_{ij}(n_x) \Delta k_x, \quad (4.4)$$

where  $\Delta k_x$  is the spacing between wavenumbers, which is equal to  $L_x/(2\pi)$ ,  $L_x$  is the  $30R$  pipe domain length, and  $N_x$  is the number of grid points in  $x$ . The discrete energy spectra are plotted as a function of the associated wavenumber  $k_x = L_x/(2\pi)n_x$  or wavelength  $\lambda_x$ . The energy spectra presented include both true wavenumber spectra based on instantaneous spatial fields of these DNS data and, for comparison, spectra from experimental hot-wire or hot-film measurements and Taylor's hypothesis to infer spatial wavenumbers based on temporal fluctuations.

A related function is the cumulative energy spectrum  $\Upsilon_{ij}(k_x = 2\pi/\Lambda_x; y)$ , which is discussed in greater detail in Guala *et al.* (2006) and Balakumar & Adrian (2007). For a given  $y$ , this is the fractional contribution to  $\overline{u'_i u'_j}$  by all wavelengths from 0 to  $\Lambda_x$  or, equivalently, all wavenumbers from  $k_x = 2\pi/\Lambda_x$  to infinity:

$$\Upsilon_{ij} \left( k_x = \frac{2\pi}{\Lambda_x}; y \right) = 1 - \frac{\int_0^{k_x} \Phi_{ij}(\tilde{k}_{x;y}) d\tilde{k}_x}{\int_0^{\infty} \Phi_{ij}(\tilde{k}_{x;y}) d\tilde{k}_x}. \quad (4.5)$$

For the discrete computed spectra,

$$\Upsilon_{ij} \left( k_x = \frac{2\pi}{\Lambda_x} = \frac{L_x}{2\pi} n_x; y \right) = 1 - \frac{\sum_{\tilde{n}_x=0}^{n_x-1} \Phi_{ij}(\tilde{n}_{x;y})}{\sum_{\tilde{n}_x=0}^{N_x/2} \Phi_{ij}(\tilde{n}_{x;y})}. \quad (4.6)$$

This definition is slightly modified from that of Guala *et al.* (2006) and Balakumar & Adrian (2007) so that in the present definition the cumulative spectrum for a

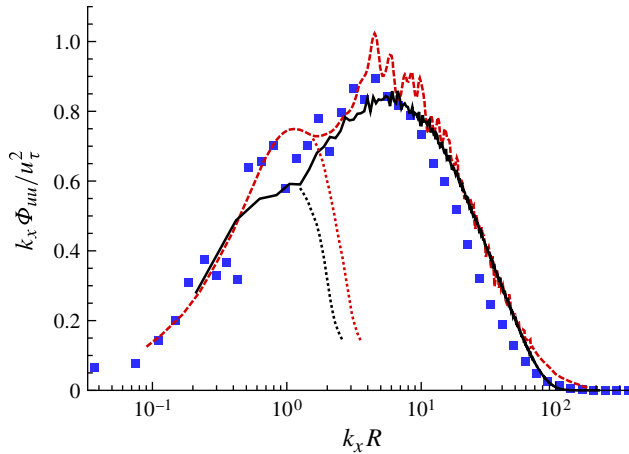


FIGURE 5. (Colour online available at [journals.cambridge.org/flm](http://journals.cambridge.org/flm)) Comparison of premultiplied energy spectra at  $y/R = 0.1$  for the present DNS at  $Re_D = 24580$  (black line) with comparable experiments: hot-wire spectra obtained by Hultmark *et al.* (2010) at  $Re_D = 25000$  (filled squares) and hot-film measurements obtained by the authors of KA99 (dashed line). The KA99 pipe flow at  $Re_{D,cl} = 33430$  based on centreline velocity is at slightly higher Reynolds number than the present DNS with  $Re_{D,cl} = 30940$ . Dotted lines depict the long-wavelength modes if the DNS and KA99 spectra were decomposed into bimodal forms, as discussed by KA99.

wavelength  $\Lambda_x$  includes the contribution of the mode with that wavelength (and all shorter wavelengths).

#### 4.2. Streamwise spectra

While the simulation's first- and second-order statistics agree closely with experimental measurements, the agreement of the DNS energy spectra with experimental spectra must be carefully examined due to possible error induced by the use of Taylor's hypothesis, as discussed in the introduction. Therefore, it is important to compare with experimental spectra obtained from a pipe at similar Reynolds number. The recent study of Hultmark *et al.* (2010) includes spectra for a pipe flow at  $Re_D = 25000$ . Otherwise, most recently obtained pipe spectra have been at higher Reynolds number than our computation. The Hultmark *et al.* (2010) premultiplied streamwise velocity spectra are compared with the present DNS in figure 5 at  $y/R = 0.1$ , which is near where a logarithmic layer would begin to form.

The spectra are generally in good agreement, with the DNS rolling off at slightly higher wavenumbers. The experimental spectra in the lower-wavenumber region are generally larger than those of the simulation, but the presence of noise that would diminish with additional statistical convergence leads to uncertainty in quantifying the difference. For this reason, an experimental pipe spectrum measured by the authors of KA99 at  $y/R = 0.1$  is also included in figure 5. This spectrum (not published in KA99) was obtained with essentially the same flow parameters as the lowest Reynolds number in KA99. We have consistently defined  $Re_D$  herein to be based on the bulk velocity, but for purposes of comparing to the KA99 spectra we note that the Reynolds number of the simulation based on centreline velocity is 30940, and that this is within 8% of the KA99 Reynolds number based on centreline velocity, 33430. We judge the two Reynolds numbers to be close enough to allow comparison of the trends. The

Kármán number for the experiment is  $R^+ = 825$  based on  $u_\tau$  calculated from pressure measurements. This value is lower than the value reported in KA99 because table 1 in KA99 used an incorrect value of the viscosity.

The experimental spectra obtained by KA99 clearly show the bimodal shape characteristic of measurements in the logarithmic layer. The lower-wavenumber peak magnitude becomes less pronounced relative to the higher-wavenumber peak with decreasing Reynolds number. In addition, the higher-wavenumber peak magnitudes of the spectra decrease slightly with decreasing Reynolds number. Since the wavenumber is scaled with  $R$  (in outer scaling), the spectral drop-off at lower  $k_x R$  is expected for the lower-Reynolds-number DNS. At high wavenumber, the DNS energy spectrum does not suffer from attenuation that potentially could affect hot-wire or hot-film spectra due to spatial averaging issues and low-pass filters typically applied. The Hultmark *et al.* (2010) spectrum rolls off at slightly lower wavenumber than the present DNS spectrum for the radius shown in figure 5, but the experiment uses a high sampling rate and small probe, so the DNS could also be responsible for the slight difference.

The behaviour of the Hultmark *et al.* (2010) spectrum at long wavelength is similar to that of the KA99 spectrum. There is evidence that a low- $k_x$  peak also appears in Hultmark *et al.* (2010) because a distinct notch separating the peaks appears between  $k_x R = 1$  and 2. The presence of noise makes the peaks' wavelengths more difficult to determine, and this is responsible for the scatter in the wavelength data points in figure 1. These points were determined by also comparing with nearby radial locations to eliminate spurious peaks.

The long-wavelength peak for the DNS appears attenuated relative to the experimental spectra, most clearly in the KA99 spectrum of figure 5 that is well converged at long wavelengths. This difference could potentially be attributed to errors affecting the experiment and the simulation relative to the true spatial wavenumber spectrum. The experiments shown for comparison are generally consistent with each other and other relevant experiments, so these are assumed to be correct representations of single-point thermal anemometer measurements. The most obvious source of the discrepancy is the use of Taylor's hypothesis to infer spatial wavenumber spectra from the measured temporal fluctuations. del Álamo & Jiménez (2009) have convincingly demonstrated the effects of this by applying a function to simulate errors introduced by the use of Taylor's hypothesis to turbulent channel DNS spectra, and the resulting spectra contain more pronounced longer-wavelength peaks that are more comparable to those of an experiment at similar Reynolds number. This will be discussed in greater depth below. Another possible source of the discrepancy is error introduced by the simulation on a finite domain length. Since the  $\langle u^2 \rangle$  statistics match very closely between simulation and experiment (as indicated by the  $u'_{x,rms}$  comparison in figure 3), and this quantity is the sum of the energies at each wavelength (as shown in (4.4)), this supports the correctness of the spectrum, with the possible issue of whether the energy could be incorrectly transferred to other modes as a result of the limited periodic domain length while the total energy remains correct. Focusing on the longest modes that are relevant to the comparison of the longer-wavelength peak and for which this could potentially be a concern, the study of Chin *et al.* (2010) for pipe simulations with a range of periodic-domain axial lengths (but at lower Reynolds number than the present simulation) indicates that the long scales generally converge even when the length is restricted. Examining the spectrum map for the long wavelengths ( $\lambda_x > 2R$ ) of the  $R^+ = 500$  pipe (their figure 7), the premultiplied energy contour lines for the lowest magnitude agree very closely with each other for the

$8\pi R$ ,  $12\pi R$  and  $20\pi R$  domain lengths. Their  $4\pi R$  domain length contour line agrees fairly well with the others for this lowest contour level, but deviates significantly from the longer domain lengths for the next higher-magnitude contour line shown in that significantly greater energy exists at wavelengths greater than about  $3R$ . Based on their spectrum map, this curve indicates an excess in energy at around  $6R$  wavelength that extends for wall-normal distances from below  $0.1R$  to above  $0.4R$  relative to the simulations on longer periodic domains and potentially could appear to be a peak at these wavelengths. The  $30R$  domain length of the present simulation is between the  $8\pi R$  and  $12\pi R$  lengths that show good agreement for Chin *et al.* (2010), and the Reynolds number of the present simulation is sufficiently close that it is not expected to dramatically alter the domain length requirements, so the evidence indicates that the computational periodic domain length of the present simulation is sufficient for reliable energy spectra at long wavelengths.

Having considered the other possibilities, the difference at long wavelength between the present DNS and the experiments appears consistent with the del Álamo & Jiménez (2009) conclusions with respect to the use of Taylor's hypothesis. However, there is evidence in the DNS that a peak may be beginning to form. Close examination reveals that the decay in the DNS spectrum with decreasing wavenumber flattens at approximately the same wavelength as where peaks are observed in experimental spectra. In the case of figure 5, this levelling occurs at  $k_x R \approx 1.2$ . Spectra at additional radii and spectrum maps demonstrate that this feature is consistent over a range of  $y$ . A more convincing long-wavelength peak occurs at higher  $y$  values for this Reynolds number, as observed in later figures, such as figure 6(b).

This long wavelength peak in the pipe DNS spectrum is similar to what occurs in the  $Re_\tau = 934$  channel DNS spectrum of del Álamo *et al.* (2004), included as grey squares in figure 2 of Monty & Chong (2009). In that figure, a dip occurs at  $\lambda_x \approx 8h$ , and a small peak exists at longer wavelength. However, Monty & Chong (2009) also compute similar spectra by zero-padding the DNS data to increase spectral resolution, and then smoothing the spectra to eliminate oscillations that are induced. This procedure appears to obscure the slight dip and longer-wavelength peak shown in the raw spectra, and they become no longer apparent. Careful examination of the  $Re_\tau = 2003$  channel energy spectra in figure 10 of del Álamo & Jiménez (2009) (particularly at  $y^+ = 200$ ) also reveals the presence of the dip and the longer-wavelength peak. The consistency of these features between simulations creates a more convincing case that they are not just noise but are characteristic of DNS spectra at relatively high Reynolds number in wall-bounded shear flows.

Returning to figure 5, the wavelength at which a short flat region or weak long-wavelength peak occurs in the DNS spectrum matches the wavelength where distinct peaks occur in the KA99 hot-film data. This supports the possibility that a small peak may be beginning to form at the correct wavelength, but the use of Taylor's hypothesis overemphasizes the energy in this region. The peak wavelengths from the DNS are included in figure 1, and they agree with peak wavelengths from the various experiments using Taylor's hypothesis. The location of the dip in the centre of the bimodal shape in the KA99 measurements also agrees well with the dip or levelling off in the DNS. The experiments indicate that the dips exist at longer wavelength for lower Reynolds number, although this variation may be restricted to relatively low Reynolds numbers. The limited domain length of the pipe (or the channel just discussed) results in Fourier modes being widely spaced for long wavelengths, since the modes occur at integer fractions of the simulation periodic wavelength (i.e.  $30R$ ,  $15R$ ,  $10R$ , ...). This wide spacing of wavelengths is apparent in

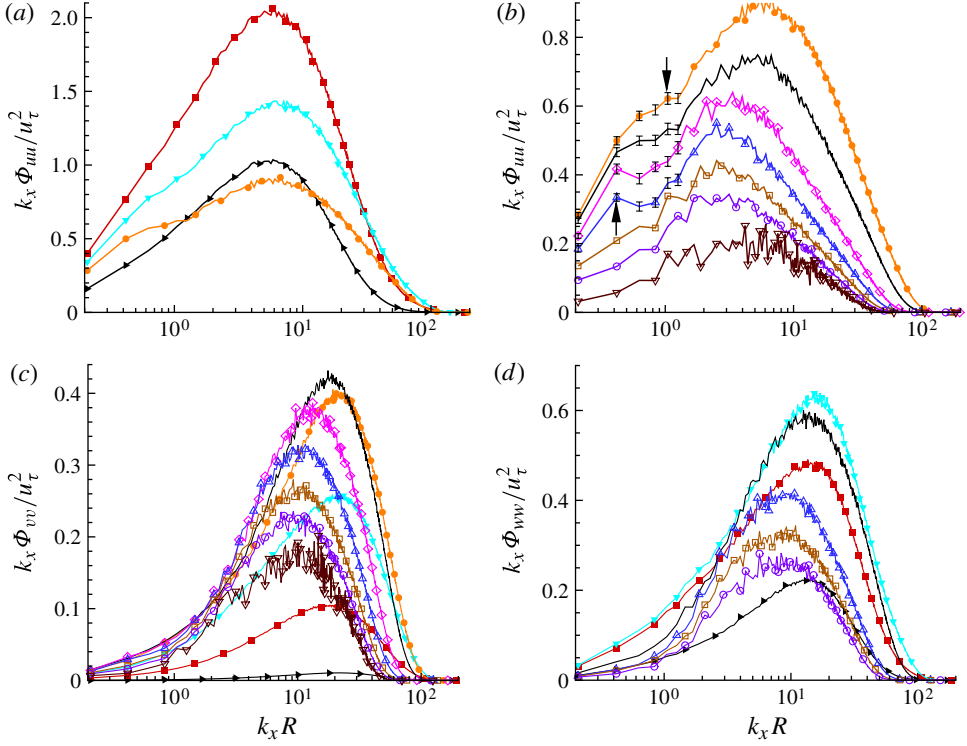


FIGURE 6. Premultiplied one-dimensional spectra as a function of streamwise wavenumber for the present DNS for each velocity component: (a)  $\Phi_{uu}$  for  $y^+ \leq 60$ ; (b)  $\Phi_{uu}$  for  $y^+ \geq 60$ ; (c)  $\Phi_{vv}$ ; and (d)  $\Phi_{ww}$ . Plots of each component share radial locations as described by table 1.

---

$y^+$	5	15	30	60	100	200	300	400	478	684
$y/R$	0.007	0.022	0.044	0.088	0.147	0.292	0.434	0.582	0.698	0.999
(a)	►	■	▼	●	—	◆	△	□	○	▽
(b)	►	■	▼	●	—	◆	△	□	○	▽
(c)	►	■	▼	●	—	◆	△	□	○	▽
(d)	►	■	▼	●	—	◆	△	□	○	▽

---

TABLE 1. Symbols for each part of figure 6.

the discrete nature of the spectral peak wavelengths of the pipe DNS reported in figure 1. However, the agreement between the spectrum maps in Chin *et al.* (2010) for the three longest domain length simulations suggests that the spectra at long wavelengths are relatively consistent despite the discrete wavelength issue. The peak location  $\lambda_x \approx 8h$  at  $y/h = 0.3$  estimated from the  $Re_\tau = 934$  channel DNS is also consistent with the data reported in figure 1.

Figure 6 presents the full set of premultiplied streamwise energy spectra from the present simulation for each velocity component. The premultiplied streamwise velocity spectra in figure 6(b) include lines representing  $y^+ = 60$  and  $y^+ = 101$ , and both possess the levelling off or slight dip identified in the  $y/R = 0.1$  ( $y^+ = 69$ ) spectrum

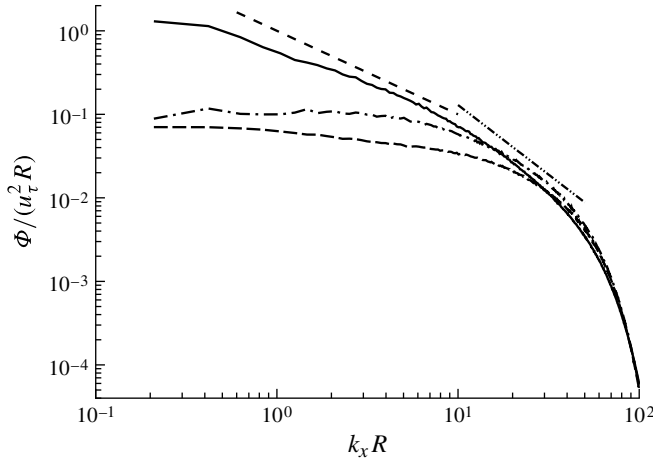


FIGURE 7. One-dimensional spectra as a function of streamwise wavenumber for the present DNS at  $y^+ = 77.5$  ( $y/R = 0.113$ ). Solid:  $\Phi_{uu}$ ; long dashed:  $\Phi_{vv}$ ; dash-dot:  $\Phi_{ww}$ ; short dashed:  $-1$  slope; dash-dot-dot:  $-5/3$  slope.

of figure 5. At lower  $y^+$  values in figure 6(a), the overall magnitudes are larger (until very near the wall), and the behaviour is dominated by the rise to the peak at  $k_x R \approx 6$ , which will be identified with the inner energy site in the discussion of figure 9. At higher  $y^+$  values in figure 6(b), the region of flattened decay transitions into a lower-wavenumber peak, with two examples indicated by arrows. Above where a logarithmic layer could be expected to occur, the lower-wavenumber peak is more comparable in magnitude to the peak at  $k_x R \approx 6$  for these radii. This indicates that these motions of such long wavelength contribute large fractions of the total energy. These wavelengths are classified as very large-scale motions, and will be discussed in further depth in connection with the spectrum maps.

In figure 7, the log-log spectra (non-premultiplied) at  $y^+ = 77.5$  for all three velocity components indicate the large amount of energy in long wavelengths of  $u$  relative to the radial and azimuthal velocity components, which have spectra that are approximately constant for low wavenumber and over an order of magnitude smaller at the lowest wavenumber (which corresponds to the wavelength of the  $30R$  periodic domain length). The viscous cutoffs at high wavenumber are similar between components. To compare the  $uu$  energy spectra with common scalings,  $-1$  and  $-5/3$  slope lines are also included. The  $uu$  spectrum appears only tangent to the  $-5/3$  line, and no clear power law is observed in the inertial subrange, probably because of the low Reynolds number.  $\Phi_{uu}$  is approximately parallel to the  $-1$  line for  $k_x R \approx 4-7$ , but, at lower wavenumbers, contains less energy than indicated by the  $-1$  line. A slight dip relative to the linear decay trend is also visible in  $\Phi_{uu}$  at  $k_x R = 1.26$  that corresponds to the dip observed in the premultiplied spectra of figure 6(b).

The premultiplied  $vv$  spectra in figure 6(c) and  $ww$  spectra in figure 6(d) clearly show a paucity of energy at low wavenumber relative to  $uu$ . The peaks occur at greater wavenumber for these velocity components than for any peak in  $uu$ . It is also clear that the peak reaches its greatest magnitude at a greater wall-normal distance for  $ww$  than  $uu$ , and at an even greater wall-normal distance for  $vv$ . These trends are more clearly shown in spectrum maps, which are now considered.



Spectrum maps depict contours of premultiplied energy as a function of wavelength and wall-normal position (del Álamo *et al.* 2004; Hutchins & Marusic 2007). In experiments on wall-bounded turbulent shear flows at high Reynolds numbers, the maps clearly reveal a bimodal distribution of  $uuu$  energy in which the maxima of the two modes visible in an energy spectrum for a particular wall-normal position correspond to two peaks clearly visible in the maps. In turbulent boundary layers, Hutchins & Marusic (2007) identified an ‘outer energy site’ that corresponds to a long-wavelength peak in the bimodal distribution that exists for a range of wall-normal locations approximately in the logarithmic layer vicinity. They identified the outer peak with superstructures, which correspond to the very large-scale motion terminology used by KA99 and others. Hutchins & Marusic (2007) also identify an ‘inner energy site’ located at the wall-normal location with maximum turbulence production and associated with the near-wall cycle (Jiménez & Pinelli 1999; Schoppa & Hussain 2002). Monty *et al.* (2009) compared spectrum maps between pipe, channel, and boundary layer flows and found these features are clearly present for each (at sufficient Reynolds number), but are most similar between pipe and channel.

The pipe spectrum map from the hot-wire study of Ng *et al.* (2011) reproduced in figure 8(a) contains the features identified by Hutchins & Marusic (2007) and Monty *et al.* (2009). This map is overlaid with premultiplied  $\Phi_{uuu}$  contours for the present DNS. Since the experimental Kármán number is 52% greater than that of the DNS (and  $Re_D$  is estimated to be 39 500), the figure contains the spectra scaled in both inner (left) and outer (right) units. In the inner-scaled plot, the inner-site peak location found by Hutchins & Marusic (2007) is marked by a black cross at  $\lambda_x^+ = 1000$  and  $y^+ = 15$  (and is assumed to be constant for these wall-bounded shear flows). The DNS contour lines suggest the peak is located slightly nearer the wall and at slightly shorter wavelength ( $\lambda_x^+ \approx 700$ ). This peak location in the DNS matches closely with the peak at  $\lambda_x^+ \approx 600$  in the  $R^+ = 500$  pipe DNS of Chin *et al.* (2010). The slight difference between the location in the present DNS and the  $\lambda_x^+ = 1000$  location approximated from experiments may be due to Reynolds number differences. The DNS contours appear similar to those of Ng *et al.* (2011) for the near-wall peak region. Along the short-wavelength extreme of the spectra, contour lines for the DNS persist to slightly smaller wavelength than for the experiment, and besides spatial averaging issues with hot-wire measurements (studied in depth by Hutchins *et al.* 2009 and Chin *et al.* 2009), this also might be attributed to numerical reasons in the simulation. Above  $y^+ \approx 50$ , the DNS  $uuu$  spectra and the experimental spectra begin to behave differently due to the different Reynolds numbers, and outer scaling is necessary for comparing outer peak features.

The outer-scaled spectrum map of figure 8(a) includes the location of the outer energy site for the experiment (black cross) and the DNS (red cross). These locations are calculated from the relationship of Mathis, Hutchins & Marusic (2009a) and Mathis *et al.* (2009b), who suggest the outer site occurs at  $y/R \simeq 3.9Re_\tau^{-1/2}$  and  $\lambda_x = 6R$ . Near the centre of the pipe ( $y/R = 1$ ), the contours match closely for both flows, except at the longest wavelengths. In the experiment, no contour island representing the local energy maximum of an outer site appears on the contour map, but the site is relatively weak for this Reynolds number (compared to the  $R^+ = 3005$  Monty *et al.* 2009 experiment in which a contour island is clearly present). Although a very small contour island may appear if the contour level is selected carefully, it is not necessary for a contour island to exist for the premultiplied spectra at individual  $y$  values to have the bimodal form. Instead, weaker longer-wavelength peaks can appear as protrusions in the contour lines to higher  $y$  values (since the spectrum in



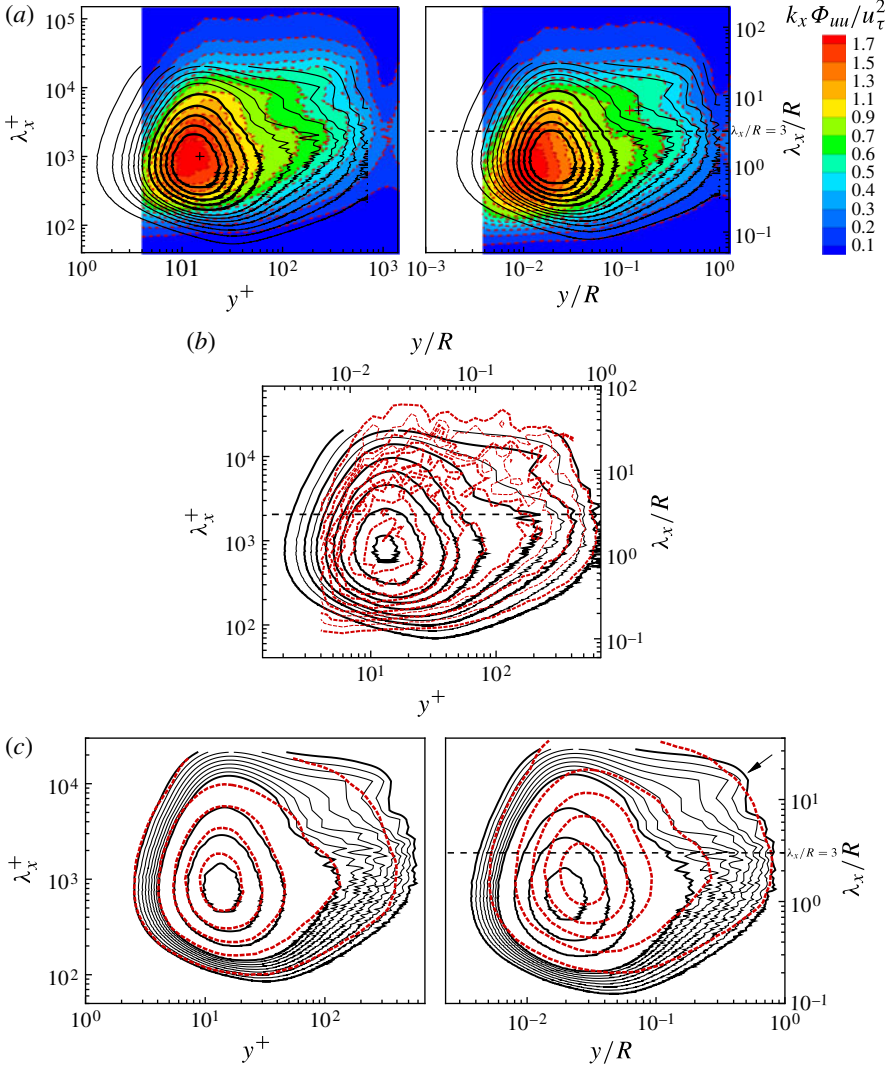


FIGURE 8. Comparisons of premultiplied  $uu$  energy maps with experiments (a,b) and a lower- $R^+$  simulation (c).  $k_x \Phi_{uu}/u_\tau^2$  contours are displayed. (a) Black contour lines for the present DNS ( $R^+ = 685$ ) are superimposed on colour contours with red dashes for hot-wire pipe spectra of Ng *et al.* (2011) at  $R^+ = 1040$ . Contour lines and colour levels correspond to values of 0.1–0.7 in increments of 0.1 (thinner lines) and 0.9–1.9 in increments of 0.2 (thicker lines). As described in the text, crosses indicate peak locations from correlations: the inner peak is black (left plot); the outer peaks are black and red for DNS and experiment, respectively (right plot). (b) Present DNS (solid black lines) and pipe-flow hot-wire measurements of Hultmark *et al.* (2010) at the same Reynolds number (dashed red lines). The thicker lines are contour levels of 0.2, 0.4, 0.6, 0.8, 1.0, 1.2, 1.6, 2.0, and the thinner lines are 0.3 and 0.5. (c) The present DNS (solid black lines) and  $R^+ = 500$  pipe-flow DNS of Chin *et al.* (2010) (dashed red lines). The dashed red lines and thick black lines are levels of 0.3, 0.7, 1.1, 1.5, 1.9, and the thin black lines are 0.35–0.65 in increments of 0.05. (a) and (c) include  $y^+$  and  $\lambda_x^+$  matched between flows for inner-scaling equivalence (left) and  $y/R$  and  $\lambda_x/R$  matched for outer equivalence (right).

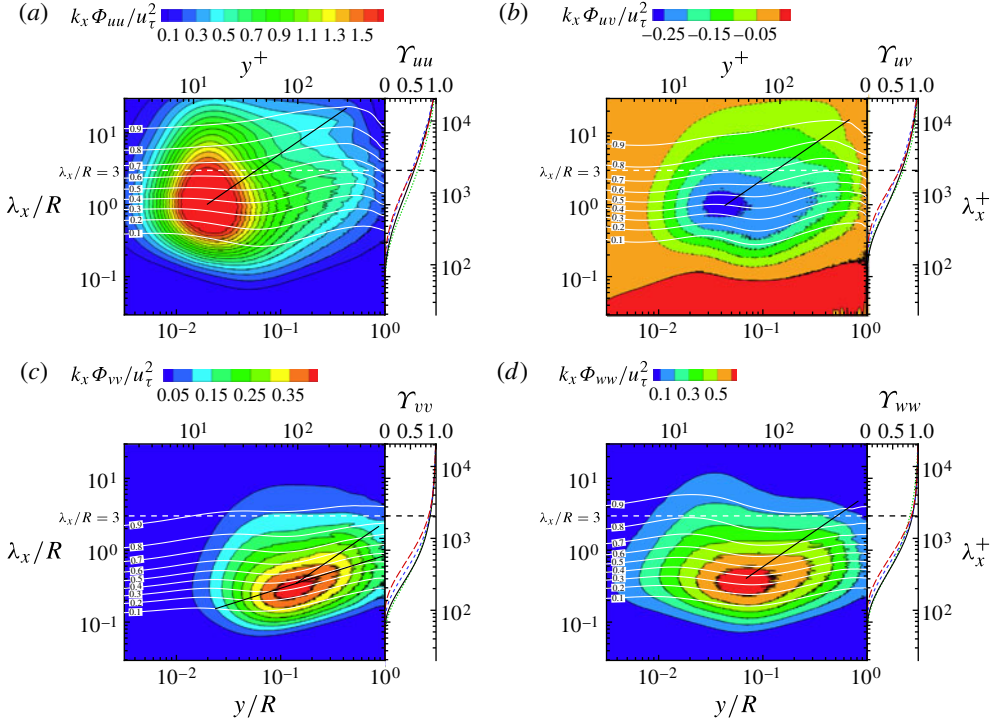


FIGURE 9. Contour maps of premultiplied spectra  $k_x \Phi(\lambda_x)$  for (a)  $uu$ , (b)  $uv$ , (c)  $vv$ , and (d)  $ww$ . Solid white lines are cumulative spectra contours at the indicated levels. Solid black lines indicate slopes of unity ( $\lambda_x \propto y$ ), with also a line along the contour major axis in (c). To the right of each map are cumulative spectra: dotted green:  $y^+ = 30, y/R = 0.044$ ; solid black: 101, 0.15; short-dashed blue: 204, 0.30; long-dashed red: 478, 0.70.

general decays with increasing  $y$ ), and this occurs for the experiment with wavelengths between 6 and  $20R$  when  $y$  is greater than  $0.06R$ . The wavelength that this feature appears to be centred about is greater than the  $6R$  suggested for the outer site, possibly as a result of the lower Reynolds number.

The DNS spectrum map in figure 8(a) is dominated by approximately concentric circular contour lines representing the decay from the peak of the inner energy site. While this characterizes the spectrum at low  $y$ , there is a notable change from sloped lines to approximately vertical contour lines as  $y$  increases for  $\lambda_x/R \approx 10$ . At  $y/R = 0.1$ , the approximately level region identified in the one-dimensional spectra is visible at  $\lambda_x/R = 5$  (which is the previously noted  $k_x R = 1.26$ ) in the line for the DNS 0.5 contour level. This location is similar to that of the protrusion noted in the Ng *et al.* (2011) spectrum. At higher  $y$  values near  $0.3R$ , the 0.4 contour line for the DNS includes a more significant protrusion that is also located near the protrusion in the experiment contour lines (to within the limited spectral resolution of the DNS spectrum).

The DNS is next compared with hot-wire spectra obtained by Hultmark *et al.* (2010) for pipe flow at the same Reynolds number as the present simulation in figure 8(b). The experimental spectra contain some noise that would reduce with further statistical convergence. The agreement between the simulation and experiment is good to within the noise. The experimental spectrum contains evidence of additional energy near the

expected outer site location that is weaker in the DNS. The apparent long-wavelength peak in the 0.4 contour line for the DNS matches closely with a similar feature in the hot-wire spectrum. The decay at high wavenumber was observed to occur at lower wavenumber for the Hultmark *et al.* (2010) spectra than the present simulation in figure 5. This is manifested in the shift of contour lines to longer wavelength for the experiment relative to the contour lines for the DNS in the region of the spectrum map where the energy decays to low magnitude as wavelength decreases.

Very near the wall (i.e.  $y^+ < 10$ ), the lowest contour levels for the experiments (figure 8*a,b*) are approximately horizontal at short wavelength, suggesting that the viscous roll-off occurs at the same wavelength in this region. In contrast, these lines for the DNS are sloped, indicating a shift to viscous decay at longer wavelength as the wall is approached. This behaviour is consistent with another pipe DNS that is compared next in figure 8*(c)*. This difference between hot-wire experiment and DNS also occurs in the turbulent channel flow study of Monty & Chong (2009). Effects of the hot wire within very small distances from the wall could contribute to this discrepancy. It is also possible that the wavelengths could be affected by Taylor's hypothesis, as del Álamo & Jiménez (2009) found that even 'small' modes with  $\lambda_x < 2h$  and  $\lambda_z < 0.4h$  in  $Re_\tau = 934$  channel simulations travel much faster than the local mean very near the wall, until  $y^+$  approaches 16 (in their figure 4). As the very long wavelengths that travel faster than the local mean are represented at shorter wavelength to overemphasize the long-wavelength peaks when  $y$  is near the logarithmic layer region and Taylor's hypothesis is used with the assumption that all motions convect at the local mean velocity, so shorter motions could be shifted to even shorter wavelength when very near the wall under the same assumptions. However, further information would be needed on the convection velocities of the very smallest wavelengths very near the wall to confirm this possibility. In figure 8*(c)*, the contour lines at short wavelength become roughly horizontal for both the present simulation and another pipe simulation at a  $y^+$  value similar to that observed in the  $Re_\tau = 934$  channel, and the behaviour at very low  $y^+$  appears consistent among simulations.

The following comparison with a pipe DNS simulation at lower Reynolds number highlights the changes with Reynolds number that may indicate an outer peak forming. Figure 8*(c)* contains a  $uu$  spectrum map for the  $R^+ = 500$  pipe simulation of Chin *et al.* (2010), who compared simulations at different pipe domain lengths, and the data digitized from the dotted line of their figure 7*(b)*, which is typical of the long domains presented ( $L_x > 8\pi R$ ). Chin *et al.* (2010) found no discernible outer-site peak. Figure 8*(c)* also contains the spectrum map for the present  $R^+ = 684.8$  DNS at the same levels. Additional levels are added to better represent the behaviour where an outer site would be expected. The contour lines for the lower Reynolds number simulation appear more circular than for the present simulation. Particularly when comparing the lowest contour level (0.3) lines, the vertical (flat with respect to wavelength) contour lines at  $\lambda_x/R \approx 10$  (below the arrow) previously discussed are absent at  $R^+ = 500$ . The additional contour lines reveal much more of the behaviour. The second-to-lowest contour level line of the  $R^+ = 500$  simulation in figure 8*(c)* reveals some deviation from a circular shape in the high- $y$ /long-wavelength quarter of the contour line, but not as much as for the present  $R^+ = 684.8$  simulation. The contour lines for the  $R^+ = 170$  pipe simulation of Chin *et al.* (2010) are even more circular. Thus, while no contour line island representing an energy peak at the outer site is visible for the present DNS, there is evidence suggesting that an outer energy site peak may be forming.

The spectrum maps for  $uu$ ,  $uv$ ,  $vv$ , and  $ww$  of the present simulation are presented in figure 9. The spectrum map in figure 9(a) displays the same data as that superimposed on figure 8. An important feature of the  $uu$  spectrum is very large-scale motions, which are defined as motions with streamwise wavelengths greater than  $3R$  based on  $uu$  energy spectrum behaviour (Balakumar & Adrian 2007). In all plots, this wavelength is indicated with a dashed line. While the vertical contour lines marking the development toward an outer energy site and protrusions from concentric ellipses appear in the  $uu$  spectra, no such features exist to any extent in the  $vv$  and  $ww$  spectra. The  $uv$  spectrum map has a slight bulge at long wavelength in the contour shapes, and this may be explained by the  $u$  influence. These spectrum contour lines and the positions where they cross the VLSM line indicate that VLSMs can make large contributions to  $uu$ , significant contributions to  $uv$ , and very minor contributions to  $vv$  and  $ww$ . Guala *et al.* (2006) suggests that large-scale structures of streamwise velocity grow in streamwise length linearly with  $y$  in the logarithmic layer. Lines with slope 1 (i.e.  $\lambda_x \propto y$ ) are included in the spectra for reference, but no convincing adherence is apparent. This is not unexpected because the Reynolds number of the present DNS does not create a sufficiently large logarithmic region. The other components also do not exhibit any notable behaviour along this line. An additional line is included on the  $vv$  map, which is unique in having an inclined principal axis of the concentric ellipses representing the peak. While the other spectra have approximately vertical or horizontal principal axes, this inclined axis indicates that dominant streamwise wavelengths of wall-normal/radial motions increase with pipe wall-normal distance in a power-law fashion that is slower than linear. When averaged,  $uu$  motions would also grow in streamwise length with increasing  $y$  because VLSMs become progressively stronger with increasing  $y$ , whereas the short-wavelength peak (inner site) dominates the behaviour near the wall. These observations are also apparent in the conventional premultiplied spectrum plots (figure 6).

The  $uu$  spectrum map has been interpreted by Hutchins & Marusic (2007) in terms of the ‘inner energy site’ being associated with strong  $u$  fluctuations and the near-wall cycle (Jiménez & Pinelli 1999; Schoppa & Hussain 2002), and the outer site being associated with VLSMs and superstructures. While the inner peak of the  $uu$  spectrum is concentrated near the wall and decays quickly with increasing  $y$ , the  $uv$  peak decays more slowly with  $y$  and peaks at a higher  $y$ . This is due to the attenuation of  $v$  fluctuation near the wall, which is seen in the  $vv$  spectrum, so the regions of  $Q2$  ( $-u, +v$ ) fluctuation (which contribute strongly to  $uv$ ) are stronger above the  $uu$  peak location. The absence of long-wavelength peaks in the  $vv$  and  $ww$  spectra indicates that these motions possess less long streamwise organization than the  $u$  motions. The  $ww$  spectrum peaks at a height intermediate between  $uu$  and  $vv$ , but also extends to near the wall. The near-wall quasi-streamwise vortices contribute strongly to  $w$  (azimuthal velocity) fluctuations (Kim, Moin & Moser 1987). The peaks of the  $vv$  and  $ww$  spectrum maps are centred at shorter wavelengths than the short-wavelength peak of the  $uu$  map. The  $uv$  peak is at a similar wavelength to that of the  $uu$  short-wavelength peak, implying that the coherence between  $u$  and  $v$  is similar to the organization leading to this peak in  $uu$ . However, energy at the outer site location is weaker in the  $uv$  spectrum map, so there is less energy at long wavelengths relative to  $uu$ . Consequently, the length scales obtained by averaging over motions of all scales are shorter for  $uv$  than  $uu$ .

Contour lines of cumulative spectra are overlaid onto the spectrum maps in figure 9. To the right of each map, cumulative spectra for selected radii are also presented in a line plot, as in Guala *et al.* (2006) and Balakumar & Adrian (2007). The

cumulative spectra quantify the previous observations of the importance of VLSM contributions, indicating that approximately 35–50 % of  $\langle uu \rangle$  is contributed by motions with wavelengths in the VLSM range. The contributions reach their maximum percentage near  $y/R \approx 0.3$ – $0.4$  but increase most rapidly with respect to  $y$  near  $y/R = 0.1$ , indicating the growing relative importance of VLSMs near the region where a logarithmic layer would be expected to occur. VLSMs remain important to  $\langle uv \rangle$ , contributing 25–40 % of the Reynolds shear stress, but make much lower contributions to the other velocity components. The contribution to  $\langle vv \rangle$  is typically less than 10 %, and the contribution to  $\langle ww \rangle$  ranges from 10 % to 20 %. Interestingly, VLSMs contribute the largest fraction to  $\langle ww \rangle$  near the wall, at  $y^+ \approx 14$ . This may be linked with the organization of quasi-streamwise vortices.

It should be noted that the definition of cumulative spectra (4.6) used to calculate the data for these plots is discrete. As discussed, the long wavelengths are coarsely spaced, so the contour lines presented are based on interpolation. Thus, at particularly long wavelengths, there is some uncertainty in cumulative energy versus wavelength. It should also be noted that the total energy in the definition includes the zero-wavenumber mode, but this mode is not included in the sum of energies of shorter wavelength in the numerator of (4.6) to calculate the cumulative energy. This places the energy at longer wavelength than the periodic domain length and therefore the zero-wavenumber mode is included with the VLSMs. This is appropriate because the zero-wavenumber mode accounts for temporal fluctuations of the spatial mean energy, and this is expected to contain energy from motions that are too long to fit in the domain length. Such motions make contributions up to 5–10 % of the energy for the  $uu$  spectra, and smaller amounts for other velocity components. This mean  $k_x = 0$  energy fraction is given as a function of radius  $r$  by

$$\frac{\langle u'^2 \rangle_{k_x=0}}{\langle u'^2 \rangle} = \frac{\langle (\langle u \rangle_{x,\theta} - \langle u \rangle)^2 \rangle}{\langle (u - \langle u \rangle)^2 \rangle}, \quad (4.7)$$

where  $u(x, r, \theta, t)$  is velocity in an instantaneous field,  $\langle \cdot \rangle_{x,\theta}(r, t)$  is the mean in only the homogeneous spatial directions for each radius of an instantaneous field, and  $\langle \cdot \rangle(r)$  is the mean in  $x, \theta$ , and time (i.e. over all fields). The cumulative  $uv$  does not strictly increase monotonically with increasing  $\Lambda$  because the  $uv$  spectrum itself is not entirely negative, but the positive contributions are very weak and at very short wavelength, so only the expected monotonic behaviour of cumulative  $uv$  is visible.

#### 4.3. Streamwise cumulative spectrum wavelengths

The cumulative spectra in figure 9 suggest plotting, as a function of radial or wall-normal position, the streamwise wavelengths  $\Lambda$  at which the cumulative spectra  $\Upsilon(\Lambda)$  are equal to chosen energy fractions. Guala *et al.* (2006) and Balakumar & Adrian (2007) plot these data for their hot-film experiments. Wavelengths for the present simulation and various pipe experiments with roughly comparable Reynolds numbers are compared in figure 10.

Several considerations involving the experimental measurements and DNS are important to interpreting the comparison. Using Taylor's hypothesis for experiments assuming all motions convect at the mean velocity has been shown to modify the energy spectrum at long wavelengths (del Álamo & Jiménez 2009), so this is expected to also affect the cumulative spectra. Monty & Chong (2009) found the issue of the weaker long-wavelength peak in DNS relative to hot-wire experiments to be of concern due to the large energies in long wavelengths noted by Guala *et al.* (2006).



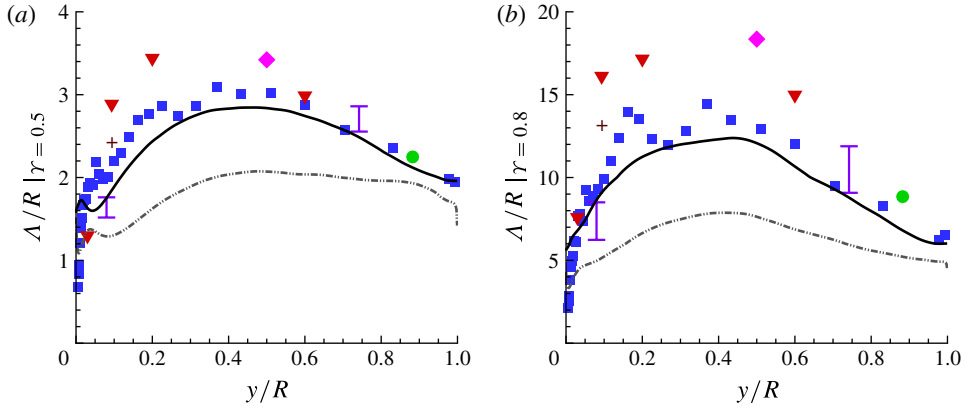


FIGURE 10. (Colour online) Wavelengths corresponding to  $uu$  and  $uv$  cumulative spectrum values of (a)  $\Upsilon = 0.5$  and (b)  $\Upsilon = 0.8$ . Black solid lines depict  $uu$  for the pipe DNS, grey dash-dot-dot lines are  $uv$  for the pipe DNS, and symbols represent  $uu$  for pipe experiments. The experiment most comparable to the present  $R^+ = 685$  ( $Re_D = 24\,580$ ) DNS is the hot-wire pipe data of Hultmark *et al.* (2010) at  $R^+ = 690$  ( $Re_D = 25\,000$ ), depicted as filled squares. The symbols for other experiments are listed in table 2. (Figure A8 in the digital appendix of Balakumar & Adrian 2007 presents a similar figure for channel and boundary layer experiments.)

Since applying Taylor's hypothesis with the assumption that all motions convect at the local mean velocity is observed to shift energy in very long wavelengths to shorter wavelengths while in the proximity of the logarithmic layer (del Álamo & Jiménez 2009), it is not immediately obvious how the cumulative spectra would be affected besides the presence of less energy at the very longest wavelengths. Guala *et al.* (2006) also commented that experimental results are subject to the limited frequency response of the data acquisition, the spatial averaging effects of the hot film, and the use of a low-pass filter that would attenuate the  $uu$  spectrum at high wavenumber. This would tend to overemphasize the fractions of energy at longer wavelength. While the Taylor's hypothesis and high-wavenumber attenuation effects do not affect the DNS, the finite domain length could affect the cumulative energy due to the coarse spacing of long wavelengths and the periodic domain possibly improperly transferring energy to various modes. However, the domain was chosen to be long relative to other simulations in order to minimize these effects.

For the present DNS (black lines in figure 10), the most relevant comparison is with the experimental pipe hot-wire measurements of Hultmark *et al.* (2010) at the same Reynolds number (filled squares). These agree well for  $y/R > 0.1$  based on the  $\Upsilon_{uu} = 0.5$  and 0.8 lines shown. While the trends match very closely, the wavelengths are somewhat larger for the hot-wire experiment relative to the present simulation. Averaging over  $y/R = 0.1$  to 1, the  $\Upsilon_{uu} = 0.5$  wavelengths are on average 6% larger and the  $\Upsilon_{uu} = 0.8$  wavelengths are 10% larger than the DNS. The experimental wavelength is greatest relative to the DNS at locations immediately above the near-wall region. Specifically, the  $\Upsilon_{uu} = 0.5$  wavelengths have the largest difference of 36% at  $y/R = 0.051$ , and the  $\Upsilon_{uu} = 0.8$  wavelengths have the largest difference of 31% at  $y/R = 0.163$ . The cumulative wavelengths for the experiment have several points that do not vary smoothly with  $y$ , but this probably would be eliminated with additional statistical convergence of the spectra. Consequently, the difference from the

DNS also contains spikes, suggesting the averages provide a better indication of the difference. Near the wall, particularly below  $y/R = 0.03$  ( $y^+ = 20$ ), the wavelengths for the experiment are significantly shorter than for the simulation. This is consistent with the differences observed and discussed in connection with the energy spectrum map of figure 8(b) and approximately matches the  $y^+$  location at which contour map lines at short wavelength for both simulation and experiment become horizontal.

The energetic importance of long-wavelength motions has been highlighted by the cumulative spectra of Guala *et al.* (2006) and Balakumar & Adrian (2007). Guala *et al.* (2006) obtained spectra experimentally for pipes with significantly higher Reynolds numbers than the present simulation, and their results indicate that  $\gamma_{uu} = 0.5$  and  $0.8$  occur at substantially longer wavelengths than for the present results. For reasons we do not fully understand, these also fall significantly above additional cumulative wavelengths that have been computed for other pipe experiments at comparable Reynolds numbers. A comparison of premultiplied spectra with those of comparable experiments (such as Perry & Abell 1975) indicates that the Guala *et al.* (2006) spectra roll off on the high wavenumber end at lower wavenumbers. Guala *et al.* (2006) commented that the spectra and cumulative distributions ‘under-represent the smallest scales of motion’ due to low-pass filtering and spatial filtering effects. However, this faster roll-off relative to other spectra begins at wavelengths significantly longer than those where Guala *et al.* (2006) suggests these effects are significant. It should be noted that plots of the wavelength of the peak VLSM energy in Guala *et al.* (2006) (also included here in figure 1) agree reasonably well with the data of Perry & Abell (1975) and Bullock *et al.* (1978). The cumulative energy plots depend on spectra over a wide range of wavenumbers besides those near the peak at long wavelength, and the differences observed could be due to distortion in the Guala *et al.* (2006) data. For this reason, their cumulative wavelengths are omitted from figure 10. We also omit a comparison with the Balakumar & Adrian (2007) cumulative wavelengths for channel experiments because of possible differences between pipe and channel flows. In general, their  $Re_\tau$  Reynolds numbers are comparable to the present simulation, and the cumulative wavelengths are of comparable magnitudes when scaled by channel half-height.

To further compare the behaviour of cumulative energy wavelengths for pipe flows, values were computed from digitized spectra for additional experiments found in the literature. These provide further support of the large amounts of energy existing at long scales, as observed by Guala *et al.* (2006). The pipe flows included for comparison are generally restricted to those with  $Re_D < 50\,000$ , and the symbols are described in table 2. One experiment with  $Re_D = 66\,000$  is also included because it includes a wide range of  $y$ . At these relatively low Reynolds numbers, the general trend is to longer wavelengths for a given cumulative energy value as Reynolds number increases, but the behaviour for a wider range of Reynolds numbers will be discussed in future work.

Various experiments include different ranges of wavenumbers. While they consistently include sufficiently small scales that the energy decays to a very low level at high wavenumbers, they vary in the degree to which the energy decays to a low level for the longest scales measured. Therefore, extrapolation was used on several data sets that did not decay as much as others, generally by extrapolating a constant non-premultiplied energy for wavenumbers below the lowest included in the data set. Other data sets did not require extrapolation, including Hultmark *et al.* (2010) and Vallikivi *et al.* (2011). The latter was obtained using a new nano-scale thermal



Symbol	Pipe flow	$R^+$	$Re_D$	Source
—	DNS	685	24 580	Present simulation
■	Hot wire	690	25 000	Hultmark <i>et al.</i> (2010)
▼	Hot wire	1606		Perry & Abell (1975)
⊥	Hot wire		49 645	Lekakis (1988)
+	Hot wire		55 000	McKeon & Morrison (2007) (figure 5a)
●	Hot wire	1133	42 700	Vallikivi <i>et al.</i> (2011) (figure 10)
◆	Hot wire	1000		Ng <i>et al.</i> (2011) (figure 9d)
---	DNS ( $uv$ )	685	24 580	Present simulation

TABLE 2. Symbols for figure 10. All  $Re_D$  values listed conform to the definition used throughout this paper based on bulk velocity. Each symbol is for  $uu$  cumulative energy except for the last row, which is for  $uv$ .

anemometry probe and is expected to also be very accurate with the smallest scales. The effect of extrapolation is illustrated by the cumulative wavelengths calculated from the data of Lekakis (1988). The cumulative spectrum wavelengths are represented as bars in figure 10, with the upper and lower ends of each bar representing the wavelengths with and without extrapolation. For these data, the change with extrapolation is relatively strong compared to other data sets. The effect is clearly larger for  $\Upsilon_{uu} = 0.8$  than 0.5, but even then the wavelengths are within  $3R$ .

Regardless of whether experiment or simulation spectra are used, all of the included data support the presence of significant fractions of energy in motions with wavelengths in the VLSM region, and the fractions would be expected to increase for higher Reynolds numbers. In the pipe flows included, the wavelengths corresponding to 50% of the  $uu$  energy occur in motions with wavelengths approaching  $3R$  for the lowest Reynolds numbers and exceeding  $3R$  for a significant fraction of the pipe cross-section for higher Reynolds numbers. It is likely that  $\Upsilon_{uu} = 0.5$  wavelengths would exceed  $3R$  if pipe simulations were performed at higher Reynolds numbers. For  $\Upsilon_{uu} = 0.8$ , the wavelengths for all of the pipe flows included reside within the VLSM range over essentially the entire  $y$  range. Thus, although there is some evidence that the Guala *et al.* (2006) calculated wavelengths were longer than accepted values due to a combination of experimental errors, and the wavelengths calculated here for the simulation and other experiments are somewhat shorter, the results strongly support the conclusion that VLSM motions are energetically important in these pipe flows for both experiments and simulations at lower Reynolds numbers. Figure 10 also shows similar trends for  $uv$  cumulative energy as for  $uu$ , except that the wavelengths are shorter. The difference between  $uu$  and  $uv$  is also consistent with experiments (Guala *et al.* 2006; Balakumar & Adrian 2007).

#### 4.4. Azimuthal spectra

Spectrum maps based on decomposition into azimuthal Fourier modes are presented in figure 11. The modes are associated with arclength wavelengths and wavenumbers, which are useful for analogy with the spanwise counterparts for channels. The arclength wavelength is defined as  $\lambda_s = 2\pi r/n_\theta$ , where  $n_\theta$  is the azimuthal mode number. The spectrum map domains are therefore curved as  $r$  reduces with increasing  $y$ . Compared to the streamwise maps (figure 9), the azimuthal maps attain their maxima at similar  $y$  locations, but differ in indicating pronounced scale growth

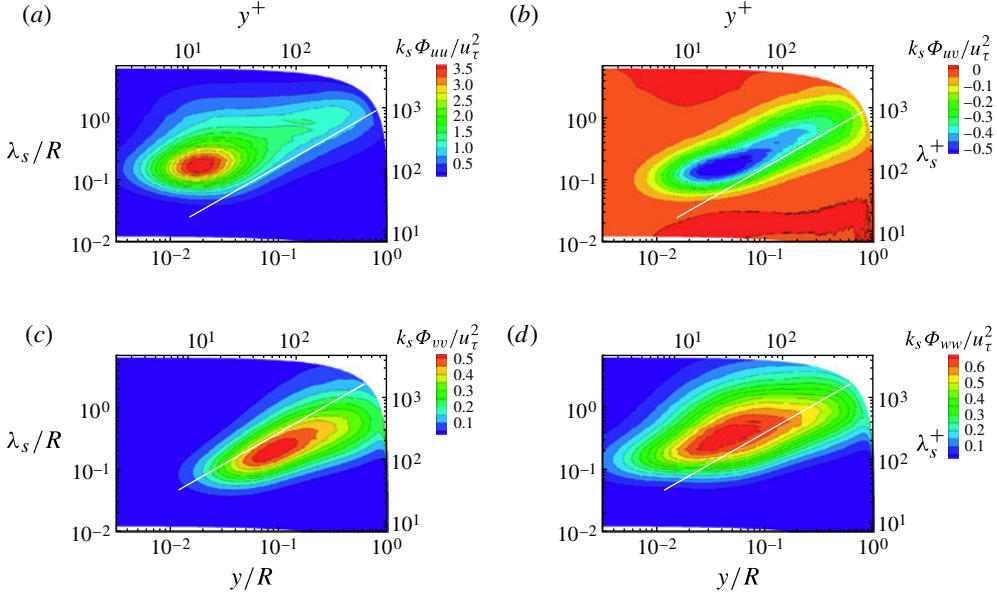


FIGURE 11. Contour maps of premultiplied one-dimensional spectra as a function of azimuthal arclength ( $s$ ) wavelength. Contour colours and black contour lines represent the premultiplied spectra for (a)  $k_s \Phi_{uu}$ , (b)  $k_s \Phi_{uv}$ , (c)  $k_s \Phi_{vv}$ , and (d)  $k_s \Phi_{ww}$ . The white lines have a slope of unity, corresponding to linear growth with  $y$ .

with  $y$ . While the strongest peak contours for the  $uu$  spectrum do not show a clear major axis, the peaks for the other components have clearly inclined major axes. The  $uu$  peak occurs at  $y^+ \approx 15$  and  $\lambda_s^+ \approx 100$ , which matches the accepted near-wall streak wavelength and supports the identification of this peak with the motions associated with quasi-streamwise vortices. This feature was also observed in azimuthal correlations from the Chin *et al.* (2010) pipe DNS. While the lower contour levels of  $uu$  are inclined in the map, there is also an apparent peak at  $y/R \approx 0.2$  and  $\lambda_s/R \approx 1$ . A similar peak is observed in the  $Re_\tau = 934$  channel DNS spanwise spectrum map of Chin *et al.* (2009) (their figure 3b), in which it occurs at  $y/h \approx 0.3$  and spanwise wavelength  $\lambda_z/h \approx 1$ . The azimuthal scale growth with  $y$  for the present pipe DNS obeys a trend similar to that observed by Tomkins & Adrian (2003), who report linear spanwise scale growth in boundary layers based on the scales of features obtained by conditional averages or their linear stochastic estimates, which are based on two-point correlations. Monty *et al.* (2007) also observe linear scale growth for the canonical flows above a certain height based on two-point correlations. While we are focused here only on the energy spectrum, these observations appear consistent with the spanwise spectrum map behaviour, and therefore lines corresponding to linear growth are superimposed on the maps. A line connecting the  $uu$  peaks has slope less than 1, consistent with the slowing growth that leads Monty *et al.* (2007) to divide the scale growth into two linear regions. Based on the major axes of the contour ellipses, the  $vv$  and  $ww$  spectra also indicate slower than linear scale growth, although the highest contour levels are inclined at approximately the correct slope for linear growth.

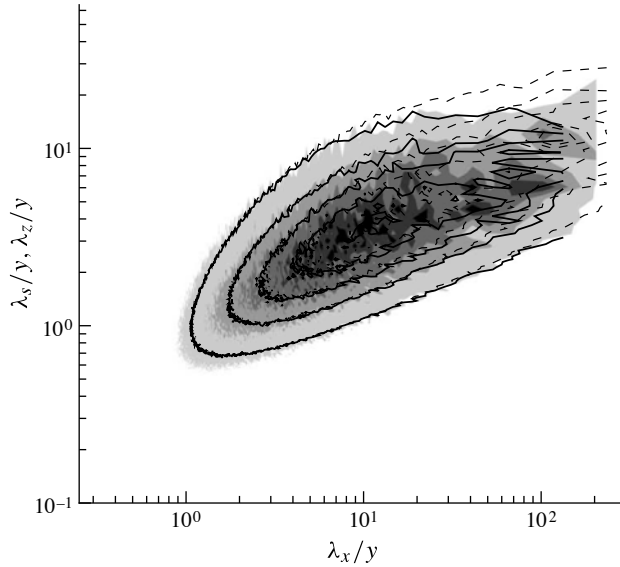


FIGURE 12. Premultiplied two-dimensional energy spectrum of streamwise velocity at  $y^+ \approx 100$ . Each spectrum is plotted at {20 %, 40 %, 60 %, 80 %, 100 %} of its value at the moderate wavelength peak. Solid black lines:  $Re_\tau = 547$  channel (del Álamo & Jiménez 2003; del Álamo *et al.* 2004); dashed black lines:  $Re_\tau = 934$  channel (del Álamo *et al.* 2004); shaded contours: present pipe (with the peak determined by applying smoothing to the spectrum, but the unsmoothed spectrum is plotted).

#### 4.5. Two-dimensional spectra

Using streamwise and azimuthal wavelengths, the two-dimensional spectrum of  $uu$  for the present DNS at  $y^+ = 101$  is presented in figure 12. Spectra from DNS simulations of channel flow at similar  $y^+$  values (matched in inner scaling) are also included, and the presentation is similar to that of del Álamo *et al.* (2004) in that the wavelengths are non-dimensionalized by  $y$ . This non-dimensionalization provides a good match between the contours, and it is also advantageous for the present comparison because it avoids assuming a relationship between  $R$  and  $h$  characterizing the different geometries. While the pipe spectrum would be smoother with better statistical convergence, the contours clearly indicate that the streamwise energy distributions by scale are very similar in the logarithmic layer region for these pipe and channel flows.

The agreement provides evidence that the effects of pipe curvature do not radically change important large-scale motion statistics at wall-normal distances up to  $\tilde{0}.15R$ , the nominal top of the logarithmic layer. At this  $y^+$  location, the two-dimensional spectrum includes peaks at moderate streamwise wavelength ( $\lambda_x/y \approx 15$ , which for the pipe is  $\lambda_x/R \approx 2$ ) and also a peak at much longer wavelength. For the pipe, this is at  $\lambda_x/R \approx 16$ , and this is probably closely related to the outer energy site in the streamwise one-dimensional spectrum maps. At this radius, there appears to be a slight shift of the shortest wavelengths to yet shorter wavelengths in both  $\lambda_x$  and  $\lambda_s$  for the pipe relative to the channel. Figure 12 and the previous spectrum comparisons also indicate that the features observed are consistent irrespective of the flow simulation

numerical method used, as the channel simulations employ spectral methods while the present pipe simulation uses finite difference.

## 5. Time evolution

The preceding results indicate strong similarities between experiment and numerical simulation of pipe flows. The issues brought up relating to Taylor's hypothesis are closely related to how the spatial fields evolve with time and the convection velocities for modes of various wavelengths. Recalling that streamwise scales of interest for VLSMs can range over  $15R$ , it is instructive to examine time sequences of streamwise velocity fluctuation contours for the full axial and azimuthal extents of the fields.

Instantaneous streamwise velocity contours for the entire periodic pipe length at  $y^+ = 80$  are visualized in figure 13 at times spaced by  $7.2R/U_{bulk}$  or  $\Delta t^+ = 275$ . The axes are scaled such that the arclength has the same scaling as axial length, although azimuthal angle  $\theta$  is displayed. Structures travelling at the bulk velocity would convect  $7.2R$  downstream between frames, or they would convect by  $6.4R$  if they travel at the local mean velocity, as is commonly assumed in conjunction with Taylor's hypothesis to infer spatial information from temporal measurements. These are relatively large time spacings, considering the findings of Dennis & Nickels (2008) when comparing instantaneous fields obtained using particle image velocimetry (PIV) with spatial fields inferred by Taylor's hypothesis from initial PIV measurements. For a turbulent boundary layer, they found that the correlation coefficient between the two decayed to 0.2 for the maximum convection distance considered of  $6.3\delta$ . However, when they calculated the correlation coefficient with filtered versions of the fields to remove the small-scale motions, it remained at 0.37 for the same convection distance, suggesting that the larger scales remain correlated over considerably longer times. Since the present study focuses on the very long scales of motion, the time spacing is appropriate to study their evolution and lifetime. While only one  $y^+$  location is presented, the consistent flat region or dip/long-wavelength peak in the one-dimensional streamwise spectrum that persists in a range wider than  $y^+ = 60$ –101 suggests that conclusions from this position should apply to this entire range.

While a description of the spatial structures is beyond the scope of this study, it is useful to identify several distinctive features and track their evolution in time. For the structures to convect downstream by the full periodic domain length of  $30R$ , a delay of between 4 and 5 frames is necessary, depending on whether the structures convect at the local mean or a higher velocity closer to the bulk velocity. Strong fluctuations are the most obvious features to visually track over long times. Examples of features are identified by circles, ellipses, and rectangles in figure 13. The circles are centred on a relatively compact but strong positive fluctuation of  $u$  velocity. The ellipses are drawn for a longer streak of positive velocity fluctuation that is initially stronger and more compact but lengthens significantly with time. Lee & Sung (2011) visualized streamwise–spanwise planes of a turbulent boundary layer simulation at a sequence of times, and they discuss the streamwise lengthening of low-speed regions that frequently occurs. They find these occurrences are associated with streamwise merging of streaks, and various scenarios are discussed by Tomkins & Adrian (2003). It has been recognized that long meandering streaks of streamwise velocity fluctuation organize such that streaks are flanked by streaks of opposite sign in the spanwise direction (Tomkins & Adrian 2003; Hutchins & Marusic 2007), and therefore observations of the lengthening of negative  $u'$  streaks may be relevant to positive  $u'$  streaks also.

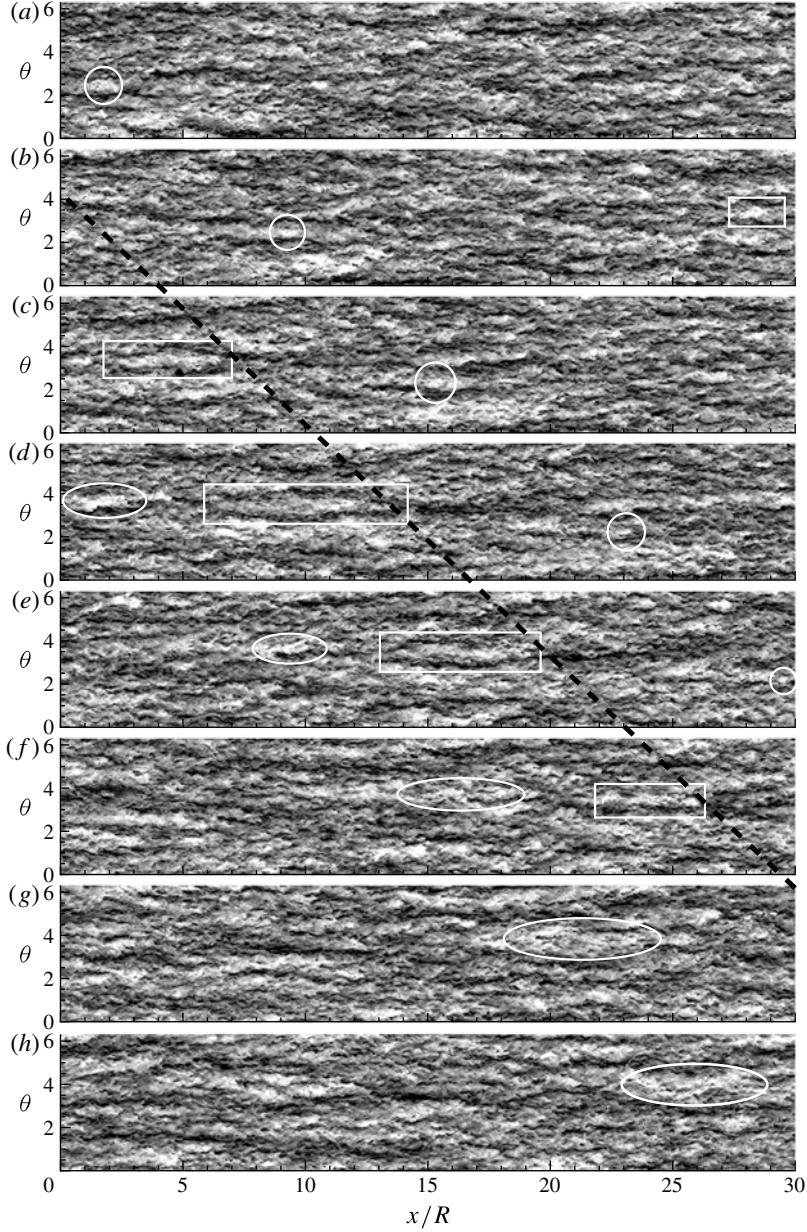


FIGURE 13. Contours of  $u'/U_{bulk}$  shaded from  $-0.2$  (black) to  $0.2$  (white) in planes at  $y^+ = 80$  with  $x/R$  and  $s/R$  equally scaled. Evenly-spaced times in terms of  $R/U_{bulk}$  are (a) 302.4; (b) 309.6; (c) 316.8; (d) 324.0; (e) 331.2; (f) 338.4; (g) 345.6; (h) 352.8.

Another interesting feature that persists over a long time is the diamond-shaped region of low-speed streaks surrounding a high-speed streak marked by a rectangle in figures 13(c) to 13(f). The downstream extents of the rectangles containing this feature are connected by a dashed black line, following Lee & Sung (2011). The slope of this line suggests a convection distance of approximately  $6.3R$  between each frame, closely



matching the mean velocity. However, the other shapes drawn for the other features indicate some variability in convection distance between each frame (convection velocity will be discussed in § 7). While the feature identified with rectangles can be visually tracked over four subsequent frames (or five frames including its embryonic stage in figure 13(b)), the feature undergoes significant changes in this duration of  $28.8R/U_{bulk}$ . If the feature from any given frame were to purely convect with no other change, the signature obtained from a single stationary point probe would be significantly different depending on which frame was chosen. Even relatively large scales sometimes change significantly when the flow has convected by only 6–7R, although in most cases the patterns in very long scales remain clearly recognizable between frames, and this becomes clearer when spatial filtering is applied.

Significant change as the flow progresses several radii downstream is consistent with the loss of correlation between measurements with and without Taylor’s hypothesis noted by Dennis & Nickels (2008), which they attributed to rapidly changing small scales. In their boundary layer at  $y/\delta = 0.16$ , they concluded visually there was strong similarity between the fields with and without Taylor’s hypothesis, but noted there were also significant differences even to large scales. The scales visually tracked in the pipe DNS are also relatively large, but the spectral analysis indicates that even longer scales that could be less visually obvious are energetically important. Several structures that were identified appear to convect at approximately the local mean velocity between neighbouring frames, but it is difficult to precisely define their centres (or other equivalent points) between frames due to the changes in structure.

To examine the very large-scale motions of interest, spatial filtering is applied to the velocity fields. Lee & Sung (2011) visualized large scales in a boundary layer field by applying a Gaussian filter. For the present pipe flow, applying Fourier filtering in the two periodic coordinates ( $x$  and  $\theta$ ) is appropriate because the structures clearly correspond to wavelengths of interest identified in the energy spectra of figure 6(b). The black arrow near the  $y^+ = 60$  premultiplied spectrum indicates the  $\lambda_x = 6R$  wavelength at which a longer-wavelength peak of the bimodal spectrum shape may begin to form. The sharp-cutoff Fourier filtering will retain this and longer-wavelength modes (the first five positive wavenumbers). Applying only streamwise filtering yields a confusing pattern, so azimuthal filtering is also performed to retain wavelengths of  $\lambda_\theta = 0.4\pi$  ( $72^\circ$  or 760 wall units at  $y^+ = 80$ ) and greater (also the first five positive wavenumbers in  $\theta$ ). This azimuthal wavelength is relatively wide, and the portion of energetic motions retained by these wavelengths is described by the two-dimensional spectrum in figure 12. Zero-wavenumber modes are also retained in the filtering. The motions these wavelengths extract are clearly VLSMs because the streamwise wavelength is well within the VLSM range ( $\lambda_x = 3R$  is the nominal cutoff). This filtering retains only significantly larger scales than that of Lee & Sung (2011).

The filtered fields in figure 14 include the same circles, ellipses, and rectangles shown in the unfiltered fields. Since much of the energy is removed when the filtering is applied, the contour levels are reduced to half of those for the unfiltered fields. The circles each have a high-speed streak in the filtered field passing through their centre, but the streamwise filtering removes the small details necessary to identify the original feature. The ellipses appear to remain centred around the strong high-speed streaks in the filtered field, although merging is evident at the last two times shown. The rectangle regions still capture the diamond-like low-speed streaks surrounding the high-speed streak, although these would probably be clearer if additional azimuthal modes were retained. The significantly differing filter lengths in  $x$  and azimuthal arclength  $s$  complicate the result. In the filtered fields, the dashed line consistently

follows the upstream sides of the low-speed streaks that are located immediately downstream of the high-speed streaks that were identified in the unfiltered fields. The filtered fields indicate that many large-scale streak features identifiable in the unfiltered fields correspond closely with long-wavelength Fourier modes, and the patterns remain visibly correlated while they convect considerable distances (though the lengths of streaks may change somewhat).

## 6. Space–time correlation

As a quantitative means of assessing the amount of change as the field evolves, we have computed the space–time correlation. Dennis & Nickels (2008) experimentally computed the space–time correlation of their turbulent boundary layer flow for spatial distances up to  $6\delta$ , but DNS allows quantification of the amount of correlation over very long convection distances. For their turbulent boundary layer simulation, Lee & Sung (2011) have calculated space–time correlations and used their inclinations to determine convection velocities. Chung & McKeon (2010) calculated spatio-temporal correlations and spatio-temporal spectra ( $k_x$ – $\omega$  spectra) for large-eddy simulations (LES) of turbulent channels with emphasis on VLSMs. From the space–time correlations, they examine the degree to which the region of strong correlation is symmetric with respect to time delay and streamwise displacement, as a symmetric correlation indicates a linear relationship and consequently Taylor’s hypothesis is valid. Since the entire periodic spatial frame of the present pipe DNS evolves in time, it is appropriate to correlate the entire  $x$ – $\theta$  plane of streamwise velocity fluctuation. The space–time correlation is

$$R_{uu}(r_x, y, \tau) = \langle u(x, \theta, y, t)u(x + r_x, \theta, y, t + \tau) \rangle, \quad (6.1)$$

where the averaging  $\langle \cdot \rangle$  includes averaging over  $x$ ,  $\theta$ , and time  $t$ .

We examine the space–time correlation at two wall-normal locations:  $y^+ = 50$  and 101. The contours in figure 15(a) focus on space–time correlation values that correspond to  $R_{uu}(r_x, y, \tau) / \langle u^2(x, \theta, y, t) \rangle$  (coefficient) values of 0.25 and less. These low fractions of the correlation maxima at  $(r_x = 0, \tau = 0)$  persist for long times. In the present correlation for unfiltered  $u$  at  $y^+ = 101$ , the lowest two contour levels correspond to correlation coefficient values of 0.10 and 0.05, and these persist for times of  $21R/U_{bulk}$  and  $42R/U_{bulk}$ , or  $\tau^+ = 810$  and 1590, respectively. In the  $Re_\tau = 2000$  LES of Chung & McKeon (2010), at  $y^+ = 98$ , a correlation coefficient of 0.14 persists for  $\tau^+ \approx 860$  and a coefficient of 0.072 persists for  $\tau^+ \approx 1270$  (when converted to viscous time units in which  $u_\tau$  is the only velocity scale). The initially rapid decay in the correlation that slows as time delay increases is observed for the correlation plotted as a function of  $r_x$  for a sequence of times in figure 15(b). The curves are spaced by the same time interval as that separating each of the contour plots in figure 13. Such rapid initial decay is consistent with Dennis & Nickels (2008), in which the correlation between velocity evolving in time and velocity estimated with Taylor’s hypothesis decays by nearly 40 % for a convection distance of  $0.05\delta$ .

The long times associated with the lower correlation values suggest that the persisting correlation is associated with the large scales of motion, such as those seen in the filtered fields of figure 14 that retain their overall configurations for substantial durations. Dennis & Nickels (2008) found that a larger fraction of the initial correlation was retained at long time delays when the fields were replaced by filtered versions. To study the VLSM scales for the present pipe flow, the same filter that was used for the visualized fields (retaining only scales no shorter than  $\lambda_x = 6R$



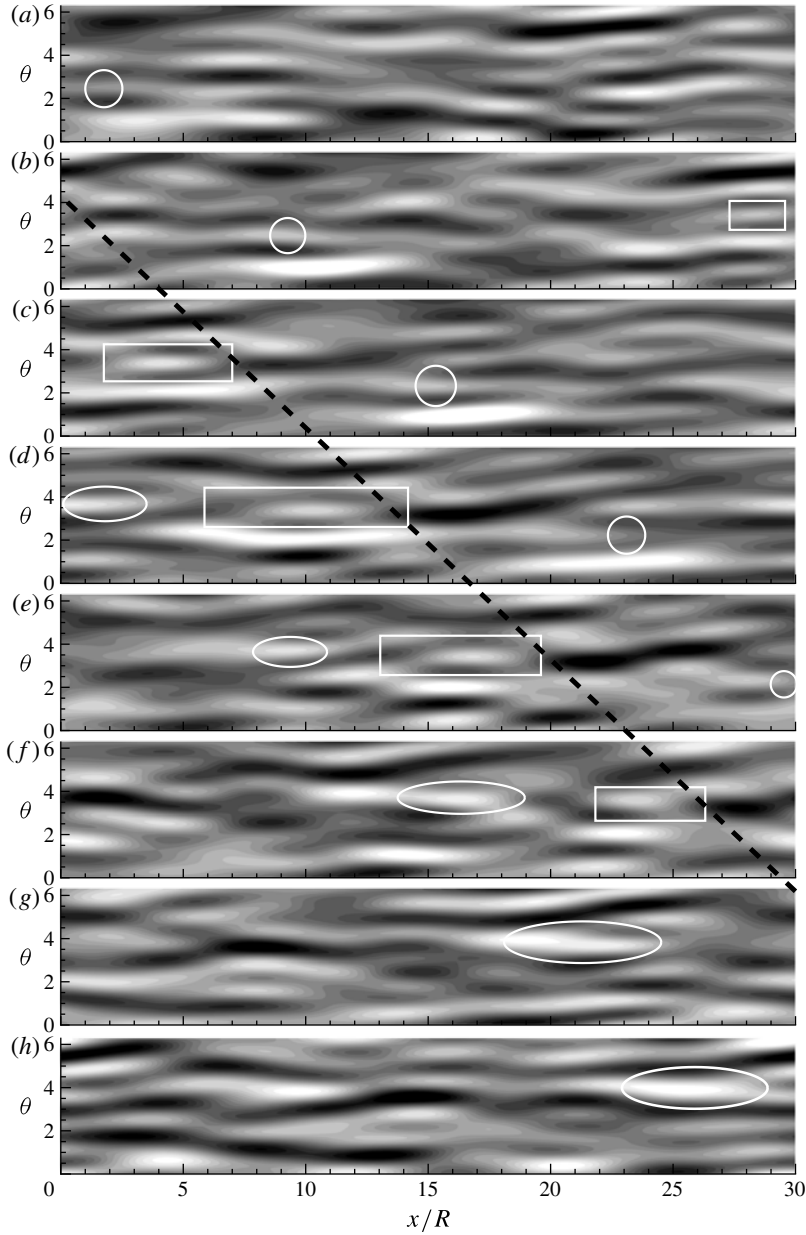


FIGURE 14. Contours of filtered  $u'/U_{bulk}$  ( $\lambda_x \geq 6R$  and  $\lambda_\theta \geq (2/5)\pi$ ) shaded from  $-0.1$  (black) to  $0.1$  (white) in planes at  $y^+ = 80$  with  $x/R$  and  $s/R$  equally scaled. Times in terms of  $R/U_{bulk}$  are (a) 302.4; (b) 309.6; (c) 316.8; (d) 324.0; (e) 331.2; (f) 338.4; (g) 345.6; (h) 352.8.

and  $\lambda_\theta = 0.4\pi$ ) was applied before calculating the correlation. Figure 15(a) shows that the correlation contours for long time delays  $\tau$  (and also long spatial shifts  $r_x$ ) approach those of the filtered version. Figure 15(b) confirms this for  $y^+ = 101$  and shows that much of the correlation is removed for small time delays by retaining

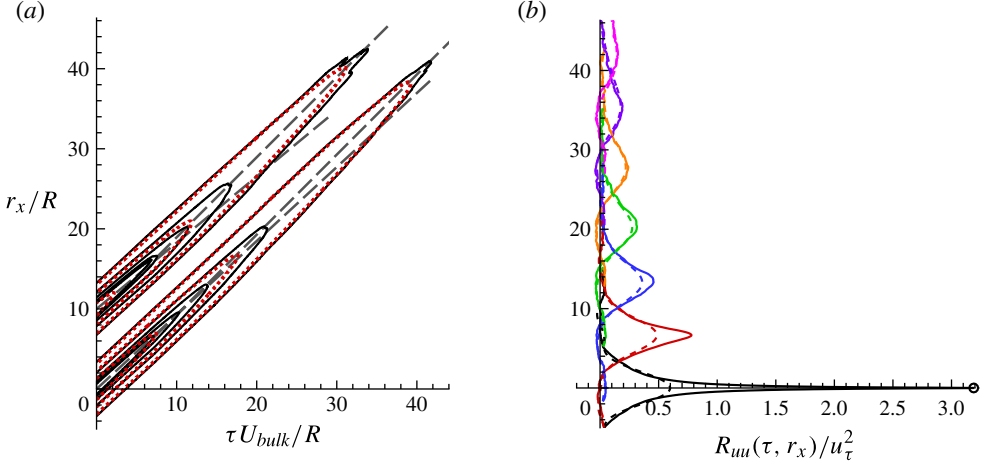


FIGURE 15. (Colour online) Space–time correlation for the present pipe simulation. (a)  $R_{uu}(\tau, r_x)/u_\tau^2$  contour lines for  $y^+ = 50$  (translated upward by 10) and  $y^+ = 101$  at contour values of  $\{0.16, 0.32, 0.48, 0.64, 0.80\}$ . Correlations at the same levels calculated between filtered versions of the same fields are also included (dashed lines), using the same filter as for figure 14. The shallower long-dashed grey lines originate at  $(\tau = 0, r_x = 0)$  and have slope equal to  $\bar{u}(y)/U_{bulk}$ . The steeper long-dashed grey lines have slope equal to unity and are positioned to pass through the major axes of the low-magnitude contour lines. (b) The unfiltered (solid line) and filtered (dashed line) correlations for  $y^+ = 101$  at  $\tau = \{0, 7.2, 14.4, 21.6, 28.8, 36, 43.2, 50.4\}R/U_{bulk}$  (peaks occur at correspondingly increasing  $r_x/R$  values). The maximum for the  $\tau = 0$  correlation is indicated by a circle.

only these very large scales, but the correlation is virtually identical with and without filtering for long time separations.

For the present pipe at  $y^+ = 50$ , the correlation decays more rapidly from the peak (along the ridge of the space–time correlation) than for  $y^+ = 101$ . It has been suggested that very large-scale motions convecting at approximately the bulk velocity have footprints extending near the wall (further discussed in § 7). If these are present along with smaller-scale motions convecting at velocities nearer the flow’s local mean, there is reduced correlation between the original field and the field at later times due to the contributions convecting at different velocities while determining a single spatial shift  $r_x$  that maximizes the correlation. The lower local mean at  $y^+ = 50$  increases this effect, consistent with the faster decay. When the correlation is scaled by a value independent of  $y$  (such as  $u_\tau^2$  or  $U_{bulk}^2$ ), the correlations decay to similar  $R_{uu}(r_x, y, \tau)/u_\tau^2$  values for long time delays (figure 15a). This occurs despite the stronger peak at  $(r_x = 0, \tau = 0)$  for  $y^+ = 50$  than for 101 (4.26 versus 3.19).

The topic of convection velocity of the motions is further discussed in § 7, but the inclination of the space–time correlation is one method of calculating convection velocity of flow quantity fluctuations (Choi & Moin 1990; Kim & Hussain 1993; Chung & McKeon 2010; Lee & Sung 2011). Kim & Hussain (1993) define propagation velocity based on this concept to be

$$c_u(y) = r_{x,max}/\tau, \quad (6.2)$$

where  $r_{x,max}$  is the axial (streamwise) displacement that maximizes the correlation  $R_{uu}(r_x, y, \tau)$  for a given time delay  $\tau$ . The  $r_{x,max}$  values are also the displacements for

the maxima of each curve in figure 15(b). To compare convection velocities, lines with slopes corresponding to convection at the bulk velocity and local mean velocity are included on the contour plots. The lines for the local mean are placed at the origin, and the major axes of the contour ellipses for higher levels appear to closely match this. However, the axes of the contours become steeper at later times, and the contours match the slope corresponding to convection at the bulk velocity. This supports the conclusion that motions of small to moderate scale (up to LSMs) account for much of the correlation at shorter times and convect at approximately the mean, but they decay so that the influence of the very large-scale motions dominates the correlations at long times. The associated convection distances are large, with correlation coefficient values of 0.05 maintained at  $y^+ = 101$  for convection distances up to  $40R$  at approximately the bulk velocity. Considering that the periodic pipe domain length is  $30R$ , this means that the correlation persists past a complete washout (based on bulk velocity). Since the space–time correlation involves an average over the entire periodic domain that conceptually repeats beyond this length, the long distance exceeding the periodic length does not directly pose any issue. However, it is not certain how the periodic boundary conditions that are imposed in  $x$  and the corresponding longest motions that the domain can accommodate could affect the behaviour of correlations at long time (and correspondingly long spatial) separations. While the spatial wavelengths are limited to  $30R$ , the longer-scale motions could appear in the time variation of the axial mean in the simulation, although the periodic domain length effects could introduce some error.

Accompanying the observed faster decay of correlation coefficient for  $y^+ = 80$  compared to  $y^+ = 101$ , the convection velocity corresponding to maximum correlation (6.2) also departs from the local mean more quickly. In figure 15(a), high space–time correlation value contours appear as concentric ellipses with the same inclination angle (Zhao & He 2009), and the inclination angles for these examples closely correspond to the local mean velocities. For lower levels, the inclination angles approach the angle corresponding to approximately the bulk velocity. This occurs as the smaller-scale motions presumably lose correlation and the faster-travelling larger motions dominate the correlation. The change in inclination from local mean velocity towards higher velocity as the space–time correlation levels decrease is clearly seen in the logarithmic layer region of the higher Reynolds number channel flow of Chung & McKeon (2010), increasing in strength as the wall is approached, whereas they convect at a velocity relatively close to the local mean further above the wall (as shown in their figure 3). In channel simulations at lower Reynolds numbers, Kim & Hussain (1993) noted that the propagation velocity calculated using this definition based on space–time correlations of velocity remained constant for a range of relatively small  $\tau$  values, except for the smallest motions for which yet smaller  $\tau$  values were used. For such channel simulations, Choi & Moin (1990) calculated space–time correlations for pressure that also curve to higher convection velocities at long time delays. At locations of more intense shear yet closer to the wall than  $y^+ = 80$ , it appears that the convection velocity may exceed the local mean even for relatively small time delays (or, equivalently, high contour values), as observed by Lee & Sung (2011) for a turbulent boundary layer at  $y^+ = 30$ .

In summary, the contours indicate that the present pipe flow remains measurably correlated (0.05 coefficient, for example) for long times that correspond to long convection distances, but the significant decay of the correlation for such time delays is attributable to both the differences in convection velocities for different scales (del Álamo & Jiménez 2009) and the small motions of the flow fields changing

significantly, thereby altering the flow relative to pure convection of the original motions (as Taylor's hypothesis would assume and was previously considered in reference to figure 13). The very long motions travelling faster than the local mean are what have been shown by del Álamo & Jiménez (2009) to shift energy from longer wavelength to overemphasize the longer wavelength peak when Taylor's hypothesis is used with the assumption that all motions convect at the local mean. This effect becomes more pronounced for the larger differences between the local mean and bulk (or centreline) velocity that occur for higher Reynolds number flows. This effect is detected in the comparison between our spectra and experiments (§ 4.2) and would be strengthened for higher Reynolds numbers.

## 7. Convection velocity

The streamwise convection velocity of motions may be calculated by several different methods besides the inclination of the space–time correlation previously considered. A variety of methods are considered by del Álamo & Jiménez (2009). The frequency–wavenumber ( $\omega$ – $k_x$ ) spectrum, which is the Fourier transform (both temporally and spatially) of the time–space correlation, allows convection velocities to be determined for individual wavelengths (or sets). Besides this method, the convection velocity of an individual (spatial) Fourier mode  $\hat{u}(k_x, k_\theta, y, t)$  expressed in terms of magnitude and phase as  $|\hat{u}(k_x, k_\theta, y, t)| \exp[i\phi(k_x, k_\theta, y, t)]$  may instantaneously be determined from  $c = -\partial_t \phi / k_x$  assuming the modes (which vary sinusoidally in both the streamwise and azimuthal directions) propagate in only the axial direction as  $u(x - ct)$ . In general, the velocity of each mode varies in time as the flow evolves, so averaging is necessary to obtain a stable velocity. We use a time average to calculate the required averages (denoted by  $\langle \cdot \rangle$ ). del Álamo & Jiménez (2009) define the average phase velocity of an individual mode as

$$c_u(k_x, k_\theta, y) = -\frac{\langle \hat{u} \hat{u}^* \partial_t \phi \rangle}{k_x \langle \hat{u} \hat{u}^* \rangle}. \quad (7.1)$$

This is exact for a monochromatic frozen wave, and the convection velocity  $c$  computed by this definition minimizes the difference between the actual time evolution of  $u(x, t)$  and a frozen wave  $u(x - ct)$  (del Álamo & Jiménez 2009). By seeking the convection velocity of frozen waves that minimizes the difference from the actual flow, del Álamo & Jiménez (2009) find that the overall convection velocity for a set of wavenumbers  $\Omega$  can be written in terms of the convection velocities of individual modes (defined in (7.1)) as

$$C_u(y) = \frac{\int_{\Omega} c_u(k_x, k_\theta, y) |\hat{u}(k_x, k_\theta, y)|^2 k_x^2 dk_x dk_\theta}{\int_{\Omega} |\hat{u}(k_x, k_\theta, y)|^2 k_x^2 dk_x dk_\theta}. \quad (7.2)$$

For the present pipe flow, we focus on the set of VLSM modes of streamwise velocity that were retained for the filtered field (figure 14):  $n_x = 1$ –5 and  $n_\theta = 1$ –5, the first five modes of positive wavenumber in each of the homogeneous directions. As previously noted, the corresponding streamwise wavelengths of  $6R$  and longer are well within the VLSM range, and the wide azimuthal modes are best for measuring the axial phase because the circumference becomes small as radius decreases, leading to uncertainty in the azimuthal phase that is assumed constant. Additional time measurements would improve the convergence of the convection velocity calculation,

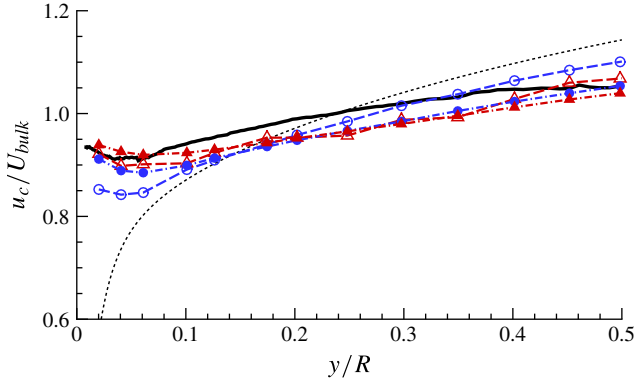


FIGURE 16. (Colour online) Comparison of axial convection velocities ( $u_c$ ) calculated for the present pipe DNS. The thick solid line represents the velocity calculated by the definition of del Álamo & Jiménez (2009) in (7.2) for the set of  $u$  modes with the five longest streamwise and five widest azimuthal wavelengths. The convection velocity is also computed from the shift corresponding to maximum space–time correlation for time delays of 7.2 (circles) and 14.4 (triangles)  $R/U_{bulk}$ . These are computed for  $R_{uu}$  calculated from velocity fields that are unfiltered (open symbols with dashed line) and filtered with the same filter as used for the instantaneous contours and space–time correlation in figure 15 (filled symbols with dash-dot line). The mean axial velocity is also shown (dotted line).

and the smoothness of the results is improved by omitting contributions at times when a mode contains very little energy (this affects the results by 3 % or less). The computed streamwise convection velocities for this VLSM mode set are plotted (thick black line) for a range of  $y$  along with the mean velocity profile of the pipe in figure 16.

The behaviour appears consistent with convection velocities reported by del Álamo & Jiménez (2009) for turbulent channel DNS. Their study included convection velocities of various Fourier spatial modes of streamwise velocity fluctuation, and they found that modes of long streamwise wavelength near the wall propagated significantly faster than the local mean velocity. With the convection velocity definition from which (7.2) was written for the present pipe flow, they calculated convection velocity for a set of modes with  $\lambda_x, \lambda_z \geq 0.25h$ . The average convection velocity in the near-wall region of a  $Re_\tau = 550$  channel flow was also calculated to be faster than the local mean in the near-wall region, but not to the extent displayed for the present pipe simulation. Probably, this is principally due to the differing sets of wavelengths for the modes that are included in each convection velocity calculation.

del Álamo & Jiménez (2009) calculate the convection velocity in their channel based on their definition for the set of modes with  $\lambda_x \geq 2h$  and  $\lambda_z \geq 0.4h$  and the set of modes with  $\lambda_x < 2h$  and  $\lambda_z < 0.4h$ . The convection velocity of the longer mode set is much greater than both that of the smaller mode set and the local mean velocity particularly when near the wall, but the longer modes are slightly slower (and also slower than the mean) when above the log layer. Near the wall, the convection velocity of our set of VLSM modes for the pipe is a significantly larger fraction of the bulk velocity than the convection velocity of the  $\lambda_x \geq 2h$  and  $\lambda_z \geq 0.4h$  set of channel modes in del Álamo & Jiménez (2009). Since their modes include somewhat shorter streamwise wavelengths than our set, this suggests that the fastest convection velocities occur for the longest modes. In (7.2), their definition strongly weights the

convection velocity of a mode set by the short-wavelength contributions. Therefore, the considerably higher convection velocities near the wall for our mode set that includes only very long motions is not unexpected.

The increase in convection velocity of  $u$  modes with increasing streamwise wavenumber is further supported by velocities calculated from  $\omega$ – $k_x$  spectra for the same flow of del Álamo & Jiménez (2009). For sets of modes with  $\lambda_z \geq 0.25h$ , the convection velocity near the wall increases with increasing streamwise wavelength for long wavelengths, although there is some scatter between different definitions (in their figure 2). Any trend to progressively greater convection velocities for the longest wavelengths (greater than  $6R$ ) is difficult to discern from spatio-temporal ( $k_x$ – $\omega$  or  $\lambda_x$ – $\lambda_t$ ) spectra, such as those of Chung & McKeon (2010), in an LES simulation of a very long channel at  $Re_\tau = 2000$ . However, they clearly find that near the wall, the motions of long streamwise wavelength propagate significantly faster than the mean velocity. Using propagation velocities calculated by (6.2) for bands of streamwise wavenumbers in a  $Re_\tau = 180$  channel, Kim & Hussain (1993) observed propagation velocity increasing with wavelength of the bands. For the present pipe simulation, at  $y < 0.15R$ , the overall trend is that the weighted average convection velocity over bands of azimuthal wavenumber index  $n_\theta = 1$ – $5$  decreases with increasing axial wavenumber index  $n_x$  values (decreasing wavelength). The  $n_x = 1$  mode set convects fastest, and the 2 and 3 mode sets convect at nearly identical (but slower than 1) rates, followed by further decreasing velocities. Since  $n_x = 1$  is the fundamental wavelength, it is not clear if the behaviour of this mode could be affected by the periodic domain length of the simulation.

LeHew, Guala & McKeon (2011) calculated convection velocities for experiments at  $y^+ = 34$  in a boundary layer by finding a line of local maxima in the  $k_x$ – $\omega$  wavenumber–frequency spectrum for streamwise velocity, and measured a different trend from the present results. In their figure 9(b), the convection velocity generally increased with increasing streamwise wavenumber (decreasing wavelength) while remaining always slightly above the local mean velocity, but this includes all spanwise scales and is nearer the wall with relatively low Reynolds number. They also include data from a boundary layer experiment of Krogstad, Kaspersen & Rimestad (1998) in which the convection velocity decreases with increasing wavenumber (decreasing wavelength), as is observed with the present simulation, but the experiment only includes relatively short wavelengths. McConachie (1981), in an experimental study of  $k_x$ – $\omega$  spectra in an  $R^+ = 2600$  turbulent pipe at  $y^+ = 70$ , found that convection velocity monotonically decreased with increasing wavenumber for all scales included.

LeHew *et al.* (2011) also computed convection velocities of individual streamwise velocity modes decomposed in both spanwise and streamwise spatial directions using a different definition of convection velocity in which an average is computed over the temporal frequencies of a frequency–wavenumber spectrum. They found from the same experiment at  $y^+ = 34$  that modes of long streamwise and wide spanwise extent were convected fastest when streamwise wavelength was between 2 and 5 boundary layer thicknesses  $\delta$ . Their results indicated that convection velocity decreased even below the local mean as streamwise wavelength further increased for a given spanwise wavelength. In the present pipe DNS, the limited averaging time leads to uncertainty in comparing individual modes. The trend among modes with long streamwise wavelength is that the convection velocity decreases with decreasing azimuthal wavelength for the widest few azimuthal modes after the fundamental ( $n_\theta = 1$ ) mode. The fundamental azimuthal mode has generally slower convection velocity. For a turbulent channel simulation, Jiménez, del Álamo & Flores (2004)



computed the convection velocity of  $\nabla^2 v$  among modes within a band of wide ( $\lambda^+ = 100\text{--}500$ ) spanwise wavelengths, and found that convection velocity increased with increasing streamwise wavelength, particularly for the longest wavelengths (their figure 7c). In a turbulent channel at  $y^+ = 15$ , del Álamo & Jiménez (2009) found that the convection velocity of  $u$  modes increases with increasing  $\lambda_x$  for a constant  $\lambda_z$  among the modes with long streamwise ( $>2h$ ) and spanwise wavelengths.

The velocities calculated by (6.2) for the spatial shift that maximizes the space–time correlation for a given time delay are also included in figure 16. They are included for time delays of  $7.2R/U_{bulk}$  and  $14.4R/U_{bulk}$ , which are quite long and for which we found the correlations to mainly consist of contributions from very long motions. For this reason, velocities calculated in this manner are also included for space–time correlations calculated from filtered  $u$  fields (as in §6) to evaluate the difference. The filter reduces the variation in the convection velocity with  $y$ , and the effect is small after the  $7.2R/U_{bulk}$  time delay. For longer time delays than  $14.4R/U_{bulk}$ , the convection velocity becomes yet more uniform in  $y$ . Calculating velocities using these time delays is different from the typical goal of minimizing the time delay (Kim & Hussain 1993), which approximates the instantaneous convection velocity. The instantaneous convection velocity is also what (7.1) seeks. However, we have restricted our calculations with (7.1) to a family of very large-scale motions that convect at relatively similar velocities and are expected to retain their overall structure for a long time, so longer time delays are acceptable for calculating phase velocity. We have similarly restricted the filtered calculation with (6.2) to the same wavelengths as when using (7.1), with the slight difference that  $k_\theta = 0$  modes are only included for the former. The differing definitions affect the velocities determined, but using the same sets of modes makes the results comparable, and figure 16 indicates that the convection velocities agree relatively closely for both definitions.

The relatively constant (in  $y$ ) convection velocities noted are suggestive of motions that remain spatially coherent in  $y$ . The evidence from the space–time correlation also suggests that they have large spatial scales in  $x$  and  $\theta$ , and that they persist for long times. Large motions extending near the wall have been noted by researchers, as summarized in del Álamo & Jiménez (2009), including del Álamo & Jiménez (2003) and del Álamo *et al.* (2004) for turbulent channel simulations. They have also been observed as ‘footprints’ extending near the wall that are strongly correlated with motions further from the wall (Hutchins & Marusic 2007; Mathis *et al.* 2009a). Although the structural forms of these motions in the present pipe flow are beyond the scope of this investigation, one structural proposal consistent with the evidence is that of a hierarchy of layers, as with the hairpin packet paradigm (Adrian 2007; Marusic & Adrian 2012), in which structures extend upward from the wall to various height scales and influence everything below their upper extents. Such structures may convect at the mean velocity at their upper (furthest from the wall) extent, as supported by Adrian, Meinhardt & Tomkins (2000) finding that hairpin head cross-sections above relatively uniform regions of low-momentum fluid on average convect at the local mean velocity of the heads. Lee & Sung (2011) support this finding for turbulent boundary layer flows in their figure 11(b). Organized groups of hairpins and the associated very long coherent motions would then propagate faster than the local mean near the wall. Using proper orthogonal decomposition of streamwise/wall-normal planes of a turbulent channel flow, Liu *et al.* (2001) found evidence of long structures far above the wall that affect the fluid near the wall and presumably would travel faster than the mean velocity near the wall. The relatively constant velocity with respect to  $y$  of these motions observed for the present pipe flow is near the bulk velocity. This suggests that



the motions propagate slightly slower than the velocity at the centreline, and figure 16 confirms this. This was also observed in the channel LES of Chung & McKeon (2010) near the centreline.

## 8. Net force spectra

Net force spectra were introduced by Guala *et al.* (2006), and their physical meaning in wall-bounded shear flow was further discussed by Balakumar & Adrian (2007). For a turbulent pipe flow, the mean flow profile is described by the Reynolds-averaged axial momentum equation in cylindrical coordinates assuming only the axial velocity component has a non-zero mean:

$$\frac{\bar{D}U}{\bar{D}t} = -\frac{1}{\rho} \frac{\partial P}{\partial x} + \frac{\nu}{r} \frac{\partial}{\partial r} \left( r \frac{\partial U}{\partial r} \right) + \frac{1}{r} \frac{\partial}{\partial r} (\overline{ru'v'}), \quad (8.1)$$

where  $\bar{D}U/\bar{D}t$  represents the total derivative of Reynolds-averaged axial velocity  $U$ ;  $u'$  and  $v'$  are velocity fluctuations in the  $x$  axial and  $-r$  wall-normal directions, respectively; and  $\partial P/\partial x$  is the mean pressure gradient. For analogy to channel flows, it is convenient to cast the equation as a function of wall-normal coordinate  $y$ :

$$\frac{\bar{D}U}{\bar{D}t} = -\frac{1}{\rho} \frac{\partial P}{\partial x} + \left( \nu \frac{\partial^2 U}{\partial y^2} - \frac{\nu}{R-y} \frac{\partial U}{\partial y} \right) + \left( \frac{\partial (-\overline{u'v'})}{\partial y} + \frac{\overline{u'v'}}{R-y} \right). \quad (8.2)$$

The terms are also split to be in a form similar to the corresponding equation for turbulent channels, which is included in Balakumar & Adrian (2007). The second term included in each parenthesis does not occur in Cartesian coordinates, and these are the only differences from the equation for channels. The terms involving the Reynolds shear stress  $\overline{u'v'}$  may be Fourier decomposed to evaluate the scales that contribute to the net forces affecting the mean velocity profile.

Guala *et al.* (2006) studied the  $\partial (-\overline{u'v'})/\partial y$  term when examining net force spectra for turbulent pipe flows, and this is the only Reynolds stress term for channels (Balakumar & Adrian 2007). It is decomposed as the integral of the co-spectrum over all wavenumbers:

$$\frac{\partial (-\overline{u'v'})}{\partial y} = \int_0^\infty \frac{\partial (-\Phi_{uv})}{\partial y} dk_x. \quad (8.3)$$

Premultiplication by  $k_x$  allows this to be presented on a logarithmic-linear plot as a function of  $k_x$  with the area under the curve to be interpreted as net force, as energy is interpreted from premultiplied spectra.

The net force spectra presented in Guala *et al.* (2006) and Balakumar & Adrian (2007) were obtained via thermal anemometry. Overall, the net force (8.3) is positive below the location of peak Reynolds stress and negative for  $y$  above this location, where its net effect is a retardation in the mean flow. All of the hot-film measurements were obtained above the peak, and the net force spectra showed that when the contributions to this term are decomposed, these generally negative terms may include positive contributions associated with long wavelengths. Such contributions are observed at wavelengths greater than  $6R$  relatively near the wall (such as  $y/R = 0.15$ ) and at sufficiently high Reynolds number (they were not observed at any of the heights measured for the  $Re_\tau = 531$  channel of Balakumar & Adrian (2007)). The observation that spectra obtained using Taylor's hypothesis (and assuming all motions convect at the local mean velocity) overemphasize energy in the long-

wavelength peak region raises questions of how these effects might impact on the sign-changing behaviour of the force spectra observed at long wavelengths for the thermal anemometry measurements. The DNS also furnishes finely spaced data in  $y$  to compute accurate derivatives (with the resolutions described in § 2), whereas the experimental accuracy of the derivatives is limited. Near the wall, experimental net force spectrum measurements are not available for comparison, as it is difficult to experimentally measure the Reynolds shear stress (the nearest measurement of Guala *et al.* (2006) was  $y/R = 0.15$ ).

The net force spectrum maps presented in figure 17 are shown with  $y$  scaled both linearly (*a*) and logarithmically (*b*). The linear axis highlights the behaviour above the near-wall region and emphasizes the fractions of the pipe radius for which various contributions dominate. Line plots are included to the right of (*a*) for comparison to the aforementioned experimental results. We plot the sum of both net Reynolds force terms (whereas Guala *et al.* 2006 focused on just the first), but it is found that the first term dominates the features visible in the plots.

The contours for the present DNS indicate that the net Reynolds force contains a strong region of positive  $-k_x(\partial\Phi_{uv}/\partial y)R/u_\tau^2$  in the buffer layer identified by A, and this is expected from the rapid increase of  $-\overline{u'v'}$  (figure 3) in this region. The colour contour levels are chosen to clearly identify the regions of various sign, but it should be noted that these levels result in significant contour saturation for some regions. While contour levels range from  $-1$  to  $1$ , the values of the present DNS for  $-k_x(\partial\Phi_{uv}/\partial y)R/u_\tau^2$  range from  $-1.1$  to  $15.6$ , with the large positive values concentrated in the region below  $y^+ = 20$ , and values for the spectrum of both net Reynolds force terms range from  $-1.8$  to  $15.5$ . Below the top of the buffer layer at  $y^+ = 30$ , indicated by a dashed black line in figure 17(*a*), all scales except the very smallest ( $\lambda_x < 0.15R$ ) accelerate the mean flow. No experimental net force spectrum measurements have been taken sufficiently close to the wall to examine this strongly accelerating regime.

The motions (termed ‘main turbulent motions’ by Balakumar & Adrian 2007) with wavelengths shorter than about  $0.5R$  (with this classification presumably dependent on Reynolds number) accelerate the mean flow from the wall up to the level of zero net force (second dashed line). This region is identified as B in the contour maps. An exception is a very weak decelerating contribution from the shortest wavelengths. The large-scale motions, with their bounding wavelengths of  $0.5R$  and  $3R$  indicated by horizontal dashed lines, accelerate the mean flow below  $y^+ = 30$ , but decelerate the mean flow – above this location. (The short-wavelength boundary of LSMs was suggested to be nominally  $0.1\pi$  times the outer length scale by Balakumar & Adrian 2007, but the distinction was not sharp.) The region of peak negative net force for LSMs above the buffer layer is identified by C and significantly weakens above  $y/R = 0.1$ .

The positive net force continues significantly above the buffer layer for wavelengths somewhat longer than the  $3R$  nominal VLSM boundary. This region is identified by D and persists to approximately  $y = 0.17R$  (or  $0.25R$  for only the first term), slightly above the nominal top of the logarithmic layer, but becomes weak. The  $y = 0.25R$  position also corresponds to the approximate location at which the axial convection velocities of the large modes with  $\lambda_x \geq 6R$  match the local mean velocity (figure 16), so it appears these very long motions that travel faster than the local mean accelerate the mean flow (i.e. are associated with a positive net force). Their contributions are particularly strong near the wall where the difference in convection velocity between the longest motions and the local mean is very large.

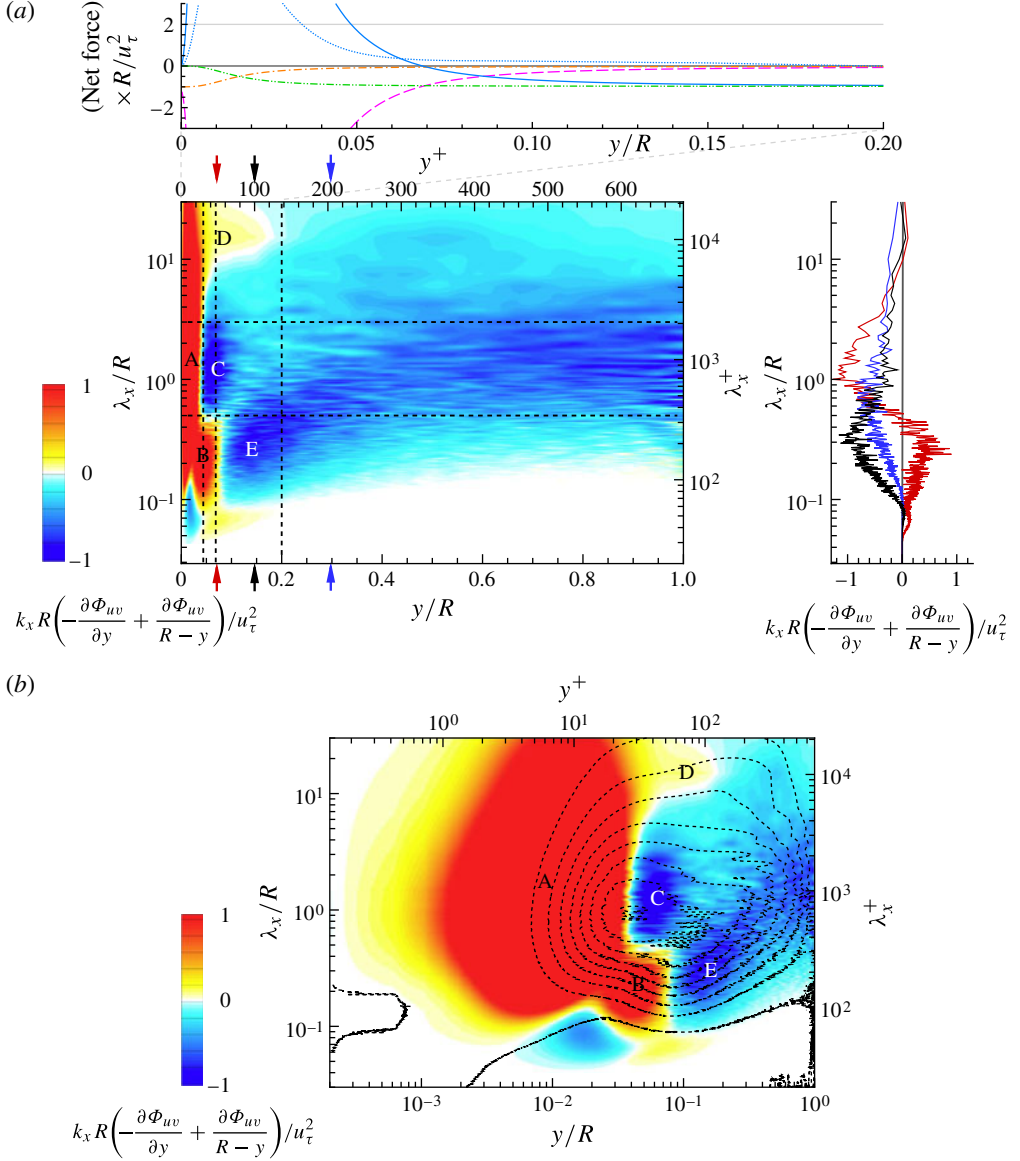


FIGURE 17. Colour contours of the sum of both net Reynolds force spectrum terms  $k_x R [-\partial \Phi_{uv}(\lambda_x, y)/\partial y + \Phi_{uv}(\lambda_x, y)/(R - y)]/u_\tau^2$  for the present DNS. (a) A linear  $y/R$  axis, and the coloured arrows are  $y$  values for similarly coloured lines in the plot to the right: red:  $y/R = 0.07$  ( $y^+ = 49$ ); black: 0.15 (101); blue: 0.30 (204). Vertical dashed black lines on the map indicate  $y^+ = 30$ ,  $y^+ = 47$  (peak Reynolds stress), and  $y/R = 0.2$ ; horizontal lines are  $\lambda_x = 3R$  and  $0.5R$ . The upper line plot is a net force balance, in which the solid grey line is  $-(1/\rho)\partial P/\partial x$ , solid light blue is  $\partial(-\overline{u'v'})/\partial y$ , dash-double-dot green is  $\overline{u'v'}/(R - y)$ , dashed magenta is  $\nu \partial^2 U/\partial y^2$ , dash-dot orange is  $-\nu/(R - y) \partial U/\partial y$ . They sum to zero. The dotted light blue line also depicts the component of  $\partial(-\overline{u'v'})/\partial y$  with  $\lambda_x \geq 6R$ . (b) A logarithmically scaled  $y/R$  axis, and  $uv$  spectrum contour lines (as in figure 9b) are overlaid for  $-k_x \Phi_{uv}(\lambda_x, y)/u_\tau^2$  of 0 : 0.033 : 0.267.

The  $y^+ = 49$  force spectrum line provides an example of the behaviour very near the peak Reynolds stress point. This position is remarkable in that the net force includes a positive peak for the shortest wavelengths, a negative region corresponding to LSM and VLSM wavelengths, and a very weak positive region at the longest wavelengths, i.e. this line passes through regions B, C, and D. The peak  $-\overline{u'v'}$  Reynolds stress occurs where the net Reynolds force  $\partial(-\overline{u'v'})/\partial y$  term of (8.2) is zero, as shown by the solid light blue line in the net force balance line plot of figure 17(a). This is equal to the spectrum of the first net Reynolds force term integrated over all wavelengths (8.3), so the peak Reynolds stress is therefore associated with the positive net Reynolds force contributions of all scales shorter than approximately  $0.55R$ . These create an accelerating net force that exactly balances the decelerating net force supported by the scales longer than  $0.55R$ , i.e. the LSMs and VLSMs, except for the very longest motions (longer than  $7.5R$ ).

At the higher location of  $y^+ = 101$ , available experimental measurements are generally consistent with the present simulation. Here, the wavelengths shorter than  $0.5R$  have switched to decelerating the flow, with a peak region of this behaviour identified as E. Thus, all wavelengths decelerate the flow except for the very longest (associated with D). This, as illustrated by the  $y^+ = 101$  line (black), matches the behaviour of the experiments in the logarithmic layer (such as at  $y/R = 0.15$ ), with negative values for high wavenumbers and a positive region for  $\lambda_x/R > 6$ . The positive region is weak for the DNS, and this is probably related to Reynolds number, as Balakumar & Adrian (2007) find no positive peak for their lowest Reynolds number (though it could exist at a lower  $y$  value than was measured). The spectrum contribution of the second net Reynolds force term also diminishes this, and the somewhat larger contributions from the first term alone are plotted in figure 18. There is also a very weak positive peak at the very highest wavenumbers that is not observed in experimental spectra and is not visually significant on the line plot for the present DNS.

The  $uv$  spectrum superimposed on the force spectrum with logarithmically scaled  $y$  shown in figure 17(b) sheds further light on the features observed. Since the first term of the net force spectrum is the partial derivative of the  $uv$  spectrum with respect to  $y$ , the regions dividing the positive and negative net force contributions are approximately where the  $uv$  spectrum remains constant with  $y$  (and the  $uv$  spectrum contour lines are parallel to the horizontal axis representing  $y$ ). The strongly positive net force near the wall is associated with the increase in the  $uv$  spectrum with  $y$  that is relatively uniform with respect to wavelength, but an indentation occurs for  $\lambda_x \approx 0.2R$  and  $y^+ \approx 20$ . As the spectrum in this region approaches a shape more similar to concentric ellipses, the associated force peaks to create the region labelled as B. The  $uv$  contributions peak in magnitude around  $y^+ = 30$  for LSM wavelengths, and the relatively rapid decline in magnitude with increasing  $y$  is associated with net force peak C. The protrusion in the  $uv$  spectrum for long wavelength that increases with  $y$  until  $y/R$  approaches 0.2 is associated with the positive net force region B. Above the  $y$  value at which peak  $-\overline{u'v'}$  occurs for each wavelength, the net force is negative as  $y$  increases. The negative net Reynolds force is particularly strong at C because it opposes the significant positive net Reynolds force of B (and a smaller contribution from D) in this region near the overall  $-\overline{u'v'}$  peak. E is offset to higher  $y$  and supports much of the negative net Reynolds force, whereas it is more uniformly distributed over a range of wavelengths for higher  $y$ . Thus, subtle features of the  $uv$  spectrum become important when the net force spectrum is examined.

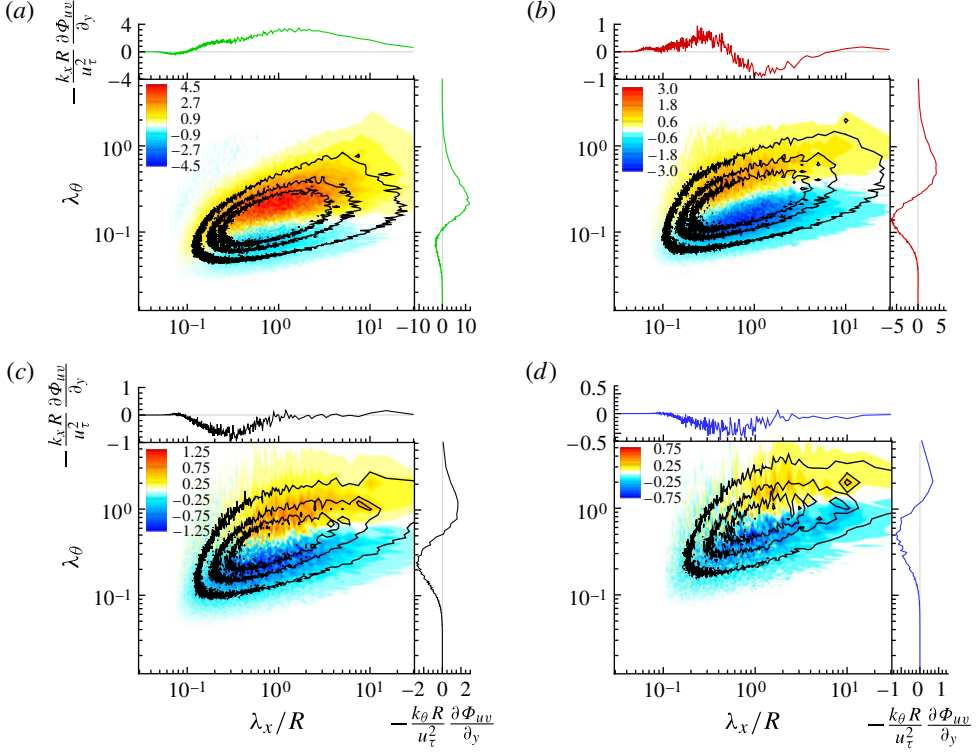


FIGURE 18. Colour contours of two-dimensional force spectra  $-k_x k_\theta R [\partial \Phi_{uv}(\lambda_x, \lambda_\theta, y) / \partial y] / u_\tau^2$  with contour lines of two-dimensional  $uv$  spectra  $-k_x k_\theta \Phi_{uv}(\lambda_x, \lambda_\theta, y) / u_\tau^2 = 0.02, 0.06, 0.1$  for the present DNS at  $y^+ =$  (a) 20; (b) 50; (c) 101; (d) 200. The one-dimensional  $x$  (to the right of each contour plot) and  $\theta$  (above each contour) force spectra are also shown, with colours matching the one-dimensional  $x$  force spectra included in figure 17(a).

In the higher  $y$  regime previously discussed in which the  $uv$  spectrum magnitude decays with increasing  $y$  for every wavelength, the behaviour matches observations for experimental spectra. In figure 17(a), the  $y^+ = 204$  line (blue) is typical of the experimental net force spectra obtained above the logarithmic layer (nominally indicated by the horizontal dashed line at 0.2) with the net force spectrum negative for all wavenumbers. The spectrum map confirms that this behaviour is consistent throughout the region sufficiently far from the wall.

The additional term  $(\overline{u'v'}) / (R - y)$  relating to Reynolds stresses in the Reynolds-averaged axial momentum equation in cylindrical coordinates (8.2) was included in the net Reynolds force plots, but the observations above can be made from the first term alone. The role of the second-term contributions is now considered. When far enough from the wall that viscous effects involving the mean axial velocity gradient are negligible, the Reynolds stress is proportional to radius:  $-\overline{u'v'} = u_\tau^2 (r/R)$ . Since this net force term is the Reynolds stress divided by the radius, the magnitude of this term is constant except in the near-wall region. When decomposed by streamwise wavelength, the distribution by wavelength remains approximately constant as  $y$  varies for  $y$  near the log-layer region and above. In this region (with values taken at  $y/R = 0.5$ ), the peak at  $\lambda_x = 1.5R$  decays to half magnitude at  $\lambda_x = 0.4R$  and  $6R$ . Summing the Fourier-decomposed Reynolds net force terms yields behaviour that

remains qualitatively very similar to only the first term (figure 17), and the peaks identified for just the first term remain. The difference most clearly visible is that the negative force region between the peak Reynolds stress location and the pipe centreline is somewhat stronger. The magnitude of the overall contribution from the second term can be assessed by integrating the net force map contributions over all wavelengths, which simply recovers the terms of the net force balance. These are plotted at the top of figure 17(a) for  $y/R$  between 0 and 0.2, above which these terms continue their asymptotic behaviour. The solid light blue line is the first  $(\partial(-\overline{u'v'})/\partial y)$  net Reynolds force term, and the dash-dot-dot green line is the second  $(\overline{u'v'})/(R - y)$ . The second term is zero near the wall and approaches a negative asymptotic value within  $y^+ = 25$ , while the first term becomes very large and positive, then becomes negative at the peak Reynolds stress point and asymptotes to the same value as the second term. Thus, the first term dominates the near-wall and buffer region, while both terms contribute equal amounts of net force away from the wall, but the wavelength distribution of the second term's contributions remains fairly consistent.

The remaining terms of the net force balance (8.2) also asymptote for large  $y$ . The first viscous term  $\nu \partial^2 U / \partial y^2$  (dashed magenta lines) becomes very strongly negative near the wall and largely balances the strongly positive first net Reynolds stress term in this region. The magnitudes of these terms are much larger than these or any other terms when away from this region, with peak magnitudes of approximately  $45u_\tau^2/R$ . For this reason, the vertical scale of the net force balance plot in figure 17 truncates the maximum scale to clearly display the terms when not in the near-wall region. The second viscous term  $-[v/(R - y)] \partial U / \partial y$  (dash-dot orange lines), which exists due to the cylindrical coordinates, is nearly zero except when  $y^+ < 20$ , and there it is much smaller than the other viscous term. While the balance between the first Reynolds force term and the first viscous force term dominates the near-wall region, further from the wall the positive net force due to the axial pressure gradient balances the first and second viscous force terms, both of which asymptote to the same value  $(-u_\tau^2/R)$ .

These Reynolds force terms may be viewed as the combined effect of motions of all length scales (as decomposed in the net force spectrum map). To assess the effect of the very large scales, the contribution to the first net Reynolds force term for  $\lambda_x \geq 6R$  is also included in the net force balance plot (dotted blue line). This length is longer than the nominal VLSM cutoff of  $3R$ , but is designed to emphasize the net accelerative force identified by Guala *et al.* (2006) for very long scales. Above  $y^+ = 30$  ( $y/R = 0.044$ ), these contributions are relatively weak for the present pipe simulation, but the previous discussion suggests that this would strengthen with increasing Reynolds number. Some of the shorter scales included in  $\lambda_x \geq 6R$  contribute negative net force for this term, which diminishes the acceleration measured for these wavelengths. At greater  $y$  values than the  $0.2R$  shown, this term becomes negative and as strong as  $-0.32u_\tau^2/R$ .

The  $\partial(-\overline{u'v'})/\partial y$  net Reynolds force term reveals further information when it is Fourier decomposed in both  $x$  and  $\theta$ . Given  $S_{ij}(k_x; k_\theta; y)$  as the two-dimensional Fourier transform of  $R_{ij}(r_x; r_\theta; y)$ , we define the one-sided cospectrum as

$$\begin{aligned} \Phi_{ij}(k_x; k_\theta; y) &= S_{ij}(k_x; k_\theta; y) + S_{ij}(-k_x; k_\theta; y) + S_{ij}(k_x; -k_\theta; y) + S_{ij}(-k_x; -k_\theta; y) \\ &= 2Re \{ S_{ij}(k_x; k_\theta; y) + S_{ij}(k_x; -k_\theta; y) \}. \end{aligned} \quad (8.4)$$

Therefore, in two dimensions, the net Reynolds force term is decomposed as

$$\frac{\partial(-\overline{u'v'})}{\partial y} = \int_0^\infty \int_0^\infty \frac{\partial(-\Phi_{uv})}{\partial y} dk_x dk_\theta. \quad (8.5)$$



The discrete form is analogous to that of the one-dimensional version in §4.1.  $\Phi_{ij}(k_x; k_\theta; y)$  and its  $y$  derivative are premultiplied by  $k_x k_\theta$  for plotting contours. Contours of the first term of the two-dimensional net force spectrum are presented in figure 18 for  $y$  positions matching the arrows in figure 17 as well as an additional position nearer the wall. The conventional one-dimensional  $\lambda_x$  spectra (shown in figure 17(a) for both net Reynolds force terms) are also included above each contour plot, and these are interpreted as the two-dimensional net force spectrum contours integrated in  $\lambda_\theta$ . One-dimensional  $\lambda_\theta$  spectra are also included to the right of each contour plot, and these are the result of integration over  $\lambda_x$ .

These two-dimensional net force spectra provide a simpler description of the motions that contribute to the one-dimensional  $\lambda_x$  net force spectra, which have been observed to occur in a somewhat complex set of regimes. The two-dimensional net force spectrum is the  $y$  derivative of the two-dimensional  $uv$  spectrum. For reference, contour lines of the actual  $uv$  spectrum are superimposed on each net force spectrum. The net Reynolds force is a sum of both of these terms, with the  $uv$  spectrum contribution weighted to decrease as the wall is approached. Contours of the  $uv$  spectrum for  $y^+ = 101$  are qualitatively similar to the  $uu$  spectrum in figure 12, except for a shift to smaller  $\lambda_\theta$  for long  $\lambda_x$  ( $>0.5R$ ). The net force spectra for all  $y$  values are similar in that each possesses an ellipse of negative net force contribution below (i.e. at shorter azimuthal wavelength than) an ellipse of positive net force contribution. The division between the regions is located at the azimuthal centre of the  $uv$  spectrum. Since the  $y$  derivative that produces the net force spectrum can be viewed as the difference between the  $uv$  spectra of two neighbouring  $y$  locations, this pattern is consistent with the shift to larger  $\lambda_\theta$  with increasing  $y$  that is apparent in the two-dimensional  $uv$  spectra shown. There is also a clear but less pronounced increase in  $\lambda_x$  wavelength with increasing  $y$ . Comparing the one-dimensional axial and azimuthal  $uv$  spectra of figures 9(b) and 11(b) illustrates the differences in scale growth with  $y$ , and the azimuthal scale growth in terms of  $\theta$  is greater than in terms of  $s$ . The strengthening and weakening of  $-\overline{u'v'}$  with increasing  $y$  also affects the net force spectrum.

Interpreting these net force spectra in terms of the various scales accelerating or decelerating the mean axial flow, for a given streamwise wavelength  $\lambda_x$ , the smaller azimuthal scales decelerate the flow while the larger azimuthal scales accelerate the flow. Given a hierarchy of scales as previously discussed (§7), this is consistent with large scales at higher  $y$  (which are large also in the azimuthal sense) accelerating the mean flow profile at lower  $y$ . This general behaviour continues for a considerable distance above the pipe wall, although the more subtle behaviour of the net force distribution in  $\lambda_x$  for a given  $\lambda_\theta$  changes. Comparing the frames of figure 18, while  $y^+ = 50$  includes the two ellipses above and below each other with similar streamwise wavelength extents, positive or negative net force regions for other locations protrude into the low- $\lambda_x$  region of the opposing net force region. The combined effect integrated over all azimuthal scales leads to the regimes of the  $\lambda_x$  spectra that were observed. The changes in  $\lambda_x$  spectra behaviour with  $y$  arise as a result of different spanwise scales of negative and positive net force dominating. The  $\lambda_\theta$  net force spectra shown to the right of each frame are more consistent in their pattern.

## 9. Conclusions

The DNS pipe flow simulation has been validated against experiments by comparisons with first- and second-order statistics, which show good agreement.

Comparisons of streamwise energy spectra between the DNS and experiments using Taylor's hypothesis reveal similar behaviour to that discussed by del Álamo & Jiménez (2009) and Monty & Chong (2009), in that long-wavelength peaks in premultiplied spectra have greater magnitude for the experiments, although the Reynolds number of the DNS limits the strength of this conclusion. The premultiplied streamwise energy spectrum provides evidence that a long-wavelength peak may be beginning to form, most convincingly above where a logarithmic layer would be expected. The peak was observed by searching for a dip or flattened region in the premultiplied spectrum, and the match between the wavelengths observed for the peak at longer wavelength and the corresponding peak in spectra obtained from experiments (figure 1) corroborates the possibility that the same phenomenon occurs in both. Comparing spectrum maps of the simulation with experiment shows that the  $y$  (or radial) position of the outer site associated with the long-wavelength peak matches the location found in experiments.

This very large-scale energy behaviour is detected in premultiplied one-dimensional spectra throughout a range of  $y$  spanning the logarithmic region, and evidence of a rudimentary peak or shoulder region exists in a much wider range. Several observations from the DNS characterize the range: in the buffer layer, the shorter-wavelength peak dominates, but a weak yet distinguishable peak relative to linear decay of the premultiplied spectrum with decreasing  $k_x$  appears. By  $y^+ = 30$  (figure 6a), this relative peak has developed into a flat region of the premultiplied spectrum. Above the logarithmic layer, the original peak location is somewhat flat by  $y^+ \approx 130$ , but a peak appears at longer wavelength. Due to the domain size, only the four discrete values of  $\lambda_x = 30R, 15R, 10R, 7.5R$  fall in the range where the long wavelength peak occurs, and the lack of spectral resolution obscures the true wavelengths of the maxima. To within the spectral resolution of the DNS, the values for the wavelength of the long-wavelength maximum agree with experiments, supporting the possible existence of long-wavelength peaks in DNS. While the wavelength at the maximum of a long-wavelength peak serves to conveniently characterize the scale of the very large-scale motions, a maximum is not necessary to see their significance. The energy contained in the VLSM range and the visualizations of very long low-speed streaks in the logarithmic layer unequivocally demonstrate the significance and existence of VLSMs.

While the importance of large- and very large-scale motions in contributing  $uu$  energy and  $uv$  shear stress has been accepted based on experiments using Taylor's hypothesis, the effects of Taylor's hypothesis require that these conclusions be re-examined. DNS results indicate that VLSMs carry large fractions of  $uu$  energy and  $uv$  shear stress for pipe flow at this Reynolds number, and the overall conclusion of the importance of VLSMs remains supported. The mean fractions of turbulent kinetic energy and Reynolds stress for each wavelength range are summarized in table 3, in which the fractions are averaged over all radii without weighting by circumference. In the region above  $y^+ = 70$ , wavelengths longer than  $3R$  account for greater than 40 % of  $uu$  energy, and greater than 30 % of  $uv$  shear stress. These values are significantly less than the 65–70 % of  $uu$  energy and 50–60 % of the  $uv$  shear stress contributions measured by Guala *et al.* (2006), due, in part, to the lower Reynolds number of the DNS. Yet, there clearly remains substantial energy in the VLSMs. The spectrum maps with superimposed cumulative fraction isolines clarify how energy is distributed among different scales for all radii.

---

Streamwise wavelength	$\langle uu \rangle$	$\langle vv \rangle$	$\langle ww \rangle$	$\langle uv \rangle$
VLSM: $\lambda_x > 3R$	0.44	0.13	0.13	0.35
LSM: $0.3R \leq \lambda_x \leq 3R$	0.51	0.69	0.72	0.61
$\lambda_x < 0.3R$	0.05	0.18	0.14	0.04

---

TABLE 3. Mean fractions of turbulent kinetic energy and Reynolds shear stress with wavelengths that are within the VLSM, LSM, and shorter ranges for the present pipe simulation. The values are computed from a linear average from the pipe axis to the wall.

---

Having established the importance of the very large-scale motions in this flow simulation and their energy spectrum properties relative to experiments, this study characterized a number of other important properties of these motions, including statistical measures of their dynamics. Space–time correlations indicate relatively rapid changes in the flow and different scale motions convecting at different velocities. Both phenomena would cause Taylor’s hypothesis with a single convection velocity to produce significant error in estimating a spatial field, even for structures barely within the VLSM range ( $3R$  long). Yet, a significant amount of energy is contributed by very large-scale motions of the flow that remain correlated for very long times and convect at approximately the bulk velocity. At  $y^+ = 101$ , for example, 5 % correlation of streamwise velocity fluctuation remains after the bulk flow convects by  $40R$ . The eddies smaller than LSMs propagate at velocities nearer the local mean, while the LSMs and VLSMs tend to propagate at velocities approaching the bulk velocity, even near the wall. The results illustrate the significant limitations that exist in inferring multiple-point statistics from single-point measurements, particularly for long scales.

Net force spectra have been calculated from the centreline down to the wall, and the results support the trends observed in experimental measurements of Guala *et al.* (2006) and Balakumar & Adrian (2007), while extending the results down to the wall. In general the net Reynolds force, given by the divergence of the Reynolds stress, is a vector field whose effects on the mean flow are much easier to understand than the Reynolds stress. The net force spectrum presents a new picture of how turbulent stresses influence the mean flow profile by accelerating the flow near the wall and decelerating the flow near the centreline. Decomposing the net Reynolds force into its spectral components makes it possible to ascertain the roles played by eddies of different scales and types. Figure 17 shows complicated behaviour at various scales. The VLSMs accelerate the mean streamwise velocity for sufficiently low  $y$  values (such as  $y/R < 0.15$ ). The net force spectra indicate that motions with approximately VLSM wavelengths, which have been found to travel much faster than the local mean near the wall, accelerate the flow in this region, while the shorter motions decelerate the flow. The smaller wavelengths coincide with known lengths of quasi-streamwise vortices and first-generation hairpin vortices, each producing second-quadrant events (Zhou *et al.* 1999; Adrian *et al.* 2000). Approaching the pipe axis, the motions with VLSM wavelengths travel somewhat slower than the local mean, and the net force spectra indicate that these decelerate the flow, as do the smaller scales. The two-dimensional force spectra in figure 18 indicate rather simple and qualitatively similar behaviour at all  $y$ -locations. For each streamwise wavelength there is a wavelength in the spanwise direction at which the net force contribution vanishes. This point always separates longer spanwise wavelengths that produce positive (accelerating) net force from shorter wavelengths that produce negative (decelerating) net force.

## Acknowledgements

The computer program used in this study was developed by the late Dr Charles D. Pierce of the Center for Turbulence Research at Stanford. X.W. was supported by the NSERC Discovery Grant and the Canada Research Chair Program (CRC) in Aeronautical Fluid Mechanics. The calculations were performed at the High Performance Computing Virtual Laboratory (HPCVL). Additional computations were performed using the Arizona State University Advanced Computing Center facilities. R.J.A. and J.R.B. gratefully acknowledge the support of the National Science Foundation with Award CBET-0933848. We gratefully acknowledge the experimental spectra provided by M. Hultmark and A. Smits, and those provided by H. Ng and J. Monty. We also wish to acknowledge J.-C. del Álamo, J. Jiménez, P. S. Zandonade, and R. D. Moser for making two-dimensional energy spectra for channel DNS available, and acknowledge C. Chin for pipe DNS spectra.

## REFERENCES

- ADRIAN, R. J. 2007 Hairpin vortex organization in wall turbulence. *Phys. Fluids* **19**, 041301.
- ADRIAN, R. J., MEINHART, C. D. & TOMKINS, C. D. 2000 Vortex organization in the outer region of the turbulent boundary layer. *J. Fluid Mech.* **422**, 1–54.
- DEL ÁLAMO, J. C. & JIMÉNEZ, J. 2001 Direct numerical simulation of the very large anisotropic scales in a turbulent channel. In *Center for Turbulence Research Annual Research Briefs*, pp. 329–341. Stanford University.
- DEL ÁLAMO, J. C. & JIMÉNEZ, J. 2003 Spectra of the very large anisotropic scales in turbulent channels. *Phys. Fluids* **15**, L41–L44.
- DEL ÁLAMO, J. C. & JIMÉNEZ, J. 2009 Estimation of turbulent convection velocities and corrections to Taylor's approximation. *J. Fluid Mech.* **640**, 5–26.
- DEL ÁLAMO, J. C., JIMÉNEZ, J., ZANDONADE, P. & MOSER, R. D. 2004 Scaling of the energy spectra of turbulent channels. *J. Fluid Mech.* **500**, 135–144.
- BAILEY, S. C. C., HULTMARK, M., SMITS, A. J. & SCHULTZ, M. P. 2008 Azimuthal structure of turbulence in high Reynolds number pipe flow. *J. Fluid Mech.* **615**, 121–138.
- BALAKUMAR, B. J. & ADRIAN, R. J. 2007 Large-and very-large-scale motions in channel and boundary-layer flows. *Phil. Trans. R. Soc. Lond. A* **365**, 665–681.
- BULLOCK, K. J., COOPER, R. E. & ABERNATHY, F. H. 1978 Structural similarity in radial correlations and spectra of longitudinal velocity fluctuations in pipe flow. *J. Fluid Mech.* **88**, 585–608.
- CHIN, C. C., HUTCHINS, N., OOI, A. S. H. & MARUSIC, I. 2009 Use of direct numerical simulation (DNS) data to investigate spatial resolution issues in measurements of wall-bounded turbulence. *Meas. Sci. Technol.* **20** (11), 115401.
- CHIN, C., OOI, A. S. H., MARUSIC, I. & BLACKBURN, H. M. 2010 The influence of pipe length on turbulence statistics computed from direct numerical simulation data. *Phys. Fluids* **22**, 115107.
- CHOI, H. & MOIN, P. 1990 On the space-time characteristics of wall-pressure fluctuations. *Phys. Fluids A* **2**, 1450–1460.
- CHUNG, D. & MCKEON, B. J. 2010 Large-eddy simulation of large-scale structures in long channel flow. *J. Fluid Mech.* **661**, 341–364.
- DENNIS, D. J. C. & NICKELS, T. B. 2008 On the limitations of Taylor's hypothesis in constructing long structures in a turbulent boundary layer. *J. Fluid Mech.* **614**, 197–206.
- EGGELS, J. G. M., UNGER, F., WEISS, M. H., WESTERWEEL, J., ADRIAN, R. J., FRIEDRICH, R. & NIEUWSTADT, F. T. M. 1994 Fully developed turbulent pipe flow: a comparison between direct numerical simulation and experiment. *J. Fluid Mech.* **268**, 175–210.
- GUALA, M., HOMMEMA, S. E. & ADRIAN, R. J. 2006 Large-scale and very-large-scale motions in turbulent pipe flow. *J. Fluid Mech.* **554**, 521–542.

- HITES, M. 1997 Scaling of high-Reynolds number turbulent boundary layers in the national diagnostic facility. PhD thesis, Illinois Institute of Technology, Chicago, IL.
- HOYAS, S. & JIMÉNEZ, J. 2006 Scaling of the velocity fluctuations in turbulent channels up to  $Re_\tau = 2003$ . *Phys. Fluids* **18**, 011702.
- HULTMARK, M., BAILEY, S. C. C. & SMITS, A. J. 2010 Scaling of near-wall turbulence in pipe flow. *J. Fluid Mech.* **649**, 103–113.
- HUTCHINS, N. & MARUSIC, I. 2007 Evidence of very long meandering features in the logarithmic region of turbulent boundary layers. *J. Fluid Mech.* **579**, 1–28.
- HUTCHINS, N., NICKELS, T. B., MARUSIC, I. & CHONG, M. S. 2009 Hot-wire spatial resolution issues in wall-bounded turbulence. *J. Fluid Mech.* **635**, 103–136.
- JIMÉNEZ, J., DEL ÁLAMO, J. C. & FLORES, O. 2004 The large-scale dynamics of near-wall turbulence. *J. Fluid Mech.* **505**, 179–199.
- JIMÉNEZ, J. & PINELLI, A. 1999 The autonomous cycle of near-wall turbulence. *J. Fluid Mech.* **389**, 335–359.
- KIM, K. C. & ADRIAN, R. J. 1999 Very large-scale motion in the outer layer. *Phys. Fluids* **11**, 417–422.
- KIM, J. & HUSSAIN, F. 1993 Propagation velocity of perturbations in turbulent channel flow. *Phys. Fluids A* **5**, 695–706.
- KIM, J., MOIN, P. & MOSER, R. 1987 Turbulence statistics in fully developed channel flow at low Reynolds number. *J. Fluid Mech.* **177**, 133–166.
- KROGSTAD, P. A., KASPERSEN, J. H. & RIMESTAD, S. 1998 Convection velocities in a turbulent boundary layer. *Phys. Fluids* **10**, 949–957.
- LEE, J. H. & SUNG, H. J. 2011 Very-large-scale motions in a turbulent boundary layer. *J. Fluid Mech.* **673**, 80–120.
- LEHEW, J., GUALA, M. & MCKEON, B. J. 2011 A study of the three-dimensional spectral energy distribution in a zero pressure gradient turbulent boundary layer. *Exp. Fluids* **51**, 997–1012.
- LEKAKIS, I. C. 1988 Coherent structures in fully developed turbulent pipe flow. PhD thesis, University of Illinois at Urbana-Champaign.
- LIU, Z.-C., ADRIAN, R. J. & HANRATTY, T. J. 2001 Large-scale modes of turbulent channel flow: transport and structure. *J. Fluid Mech.* **448**, 53–80.
- MARUSIC, I. & ADRIAN, R. J. 2012 Scaling issues and the role of organized motion in wall turbulence. In *Ten Chapters in Turbulence* (ed. P. A. Davidson, Y. Kaneda & K. R. Sreenivasan). Cambridge University Press.
- MARUSIC, I., MCKEON, B. J., MONKEWITZ, P. A., NAGIB, H. M., SMITS, A. J. & SREENIVASAN, K. R. 2010 Wall-bounded turbulent flows at high Reynolds numbers: Recent advances and key issues. *Phys. Fluids* **22**, 065103.
- MATHIS, R., HUTCHINS, N. & MARUSIC, I. 2009a Large-scale amplitude modulation of the small-scale structures in turbulent boundary layers. *J. Fluid Mech.* **628**, 311–337.
- MATHIS, R., MONTY, J. P., HUTCHINS, N. & MARUSIC, I. 2009b Comparison of large-scale amplitude modulation in turbulent boundary layers, pipes, and channel flows. *Phys. Fluids* **21**, 111703.
- MCCONACHIE, P. J. 1981 The distribution of convection velocities in turbulent pipe flow. *J. Fluid Mech.* **103**, 65–85.
- MCKEON, B. J. & MORRISON, J. F. 2007 Asymptotic scaling in turbulent pipe flow. *Phil. Trans. R. Soc. Lond. A* **365**, 771–787.
- MOIN, P. 2009 Revisiting Taylor's hypothesis. *J. Fluid Mech.* **640**, 1–4.
- MONTY, J. P. & CHONG, M. S. 2009 Turbulent channel flow: comparison of streamwise velocity data from experiments and direct numerical simulation. *J. Fluid Mech.* **633**, 461–474.
- MONTY, J. P., HUTCHINS, N., NG, H. C. H., MARUSIC, I. & CHONG, M. S. 2009 A comparison of turbulent pipe, channel and boundary layer flows. *J. Fluid Mech.* **632**, 431–442.
- MONTY, J. P., STEWART, J. A., WILLIAMS, R. C. & CHONG, M. S. 2007 Large-scale features in turbulent pipe and channel flows. *J. Fluid Mech.* **589**, 147–156.
- NG, H. C. H., MONTY, J. P., HUTCHINS, N., CHONG, M. S. & MARUSIC, I. 2011 Comparison of turbulent channel and pipe flows with varying Reynolds number. *Exp. Fluids* **51**, 1261–1281.

- PERRY, A. E. & ABELL, C. J. 1975 Scaling laws for pipe-flow turbulence. *J. Fluid Mech.* **67**, 257–271.
- SCHOPPA, W. & HUSSAIN, F. 2002 Coherent structure generation in near-wall turbulence. *J. Fluid Mech.* **453**, 57–108.
- SREENIVASAN, K. R. 1987 A unified view of the origin and morphology of the turbulent boundary layer structure. In *Turbulence Management and Relaminarization* (ed. H. W. Liepmann & R. Narasimha). pp. 37–61. Springer.
- SREENIVASAN, K. R. & SAHAY, A. 1997 The persistence of viscous effects in the overlap region, and the mean velocity in turbulent pipe and channel flows. In *Self-Sustaining Mechanisms of Wall Turbulence* (ed. R. Panton). pp. 253–272. Computational Mechanics Publications.
- TAYLOR, G. I. 1938 The spectrum of turbulence. *Proc. R. Soc. Lond.* **164** (919), 476–490.
- TOMKINS, C. D. & ADRIAN, R. J. 2003 Spanwise structure and scale growth in turbulent boundary layers. *J. Fluid Mech.* **490**, 37–74.
- DEN TOONDER, J. M. J. & NIEUWSTADT, F. T. M. 1997 Reynolds number effects in a turbulent pipe flow for low to moderate Re. *Phys. Fluids* **9**, 3398–3409.
- TOWNSEND, A. A. 1976 *The Structure of Turbulent Shear Flow*, 2nd edn. Cambridge University Press.
- VALLIKIVI, M., HULTMARK, M., BAILEY, S. C. C. & SMITS, A. J. 2011 Turbulence measurements in pipe flow using a nano-scale thermal anemometry probe. *Exp. Fluids* **51**, 1521–1527.
- WU, X. & MOIN, P. 2008 A direct numerical simulation study on the mean velocity characteristics in turbulent pipe flow. *J. Fluid Mech.* **608**, 81–112.
- ZHAO, X. & HE, G.-W. 2009 Space-time correlations of fluctuating velocities in turbulent shear flows. *Phys. Rev. E* **79**, 046316.
- ZHOU, J., ADRIAN, R. J., BALACHANDAR, S. & KENDALL, T. M. 1999 Mechanisms for generating coherent packets of hairpin vortices in channel flow. *J. Fluid Mech.* **387**, 353–396.